

PHOTOGRAPH THIS SHEET

AD-A227 444

DTIC ACCESSION NUMBER

LEVEL

INVENTORY

DNA-TR-86-306

DOCUMENT IDENTIFICATION

1 Sep 1986

DISTRIBUTION STATEMENT A

Approved for public release;
Distribution Unlimited

DISTRIBUTION STATEMENT

ACCESSION FOR

NTIS GRA&I
DTIC TRAC
UNANNOUNCED
JUSTIFICATION

BY

DISTRIBUTION/

AVAILABILITY CODES

DISTRIBUTION

AVAILABILITY AND/OR SPECIAL

A-1

DISTRIBUTION STAMP

DTIC
COPY
INSPECTED
4

DTIC
ELECTE
OCT 10 1990
S E D

DATE ACCESSIONED

DATE RETURNED

90 10 0 027

DATE RECEIVED IN DTIC

REGISTERED OR CERTIFIED NUMBER

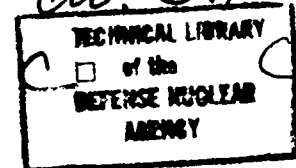
PHOTOGRAPH THIS SHEET AND RETURN TO DTIC-FDAC

AD-A227 444

DNA-TR-86-306

INTERPRETATION OF GAS TURBINE RESPONSE DUE TO DUST INGESTION

Paul F. Batcho, et al.
Calspan Advanced Technology Center
P. O. Box 400
Buffalo, NY 14225-0400



3 NOV 1987

1 September 1986

Technical Report

CONTRACT No. DNA 001-83-C-0182

Approved for public release;
distribution is unlimited.

THIS WORK WAS SPONSORED BY THE DEFENSE NUCLEAR AGENCY
UNDER RDT&E RMSS CODE B342085466 N99QMXAJ00002 H2590D.

Prepared for
Director
DEFENSE NUCLEAR AGENCY
Washington, DC 20305-1000

Destroy this report when it is no longer needed. Do not return to sender.

PLEASE NOTIFY THE DEFENSE NUCLEAR AGENCY
ATTN: TITL, WASHINGTON, DC 20305 1000, IF YOUR
ADDRESS IS INCORRECT, IF YOU WISH IT DELETED
FROM THE DISTRIBUTION LIST, OR IF THE ADDRESSEE
IS NO LONGER EMPLOYED BY YOUR ORGANIZATION.



DISTRIBUTION LIST UPDATE

This mailer is provided to enable DNA to maintain current distribution lists for reports. We would appreciate your providing the requested information.

- ☐ Add the individual listed to your distribution list.
- ☐ Delete the cited organization/individual.
- ☐ Change of address.

NAME: _____

ORGANIZATION: _____

OLD ADDRESS

CURRENT ADDRESS

TELEPHONE NUMBER: () _____

SUBJECT AREA(s) OF INTEREST:

DNA OR OTHER GOVERNMENT CONTRACT NUMBER: _____

CERTIFICATION OF NEED-TO-KNOW BY GOVERNMENT SPONSOR (if other than DNA):

SPONSORING ORGANIZATION: _____

CONTRACTING OFFICER OR REPRESENTATIVE: _____

SIGNATURE: _____

CUT HERE AND RETURN



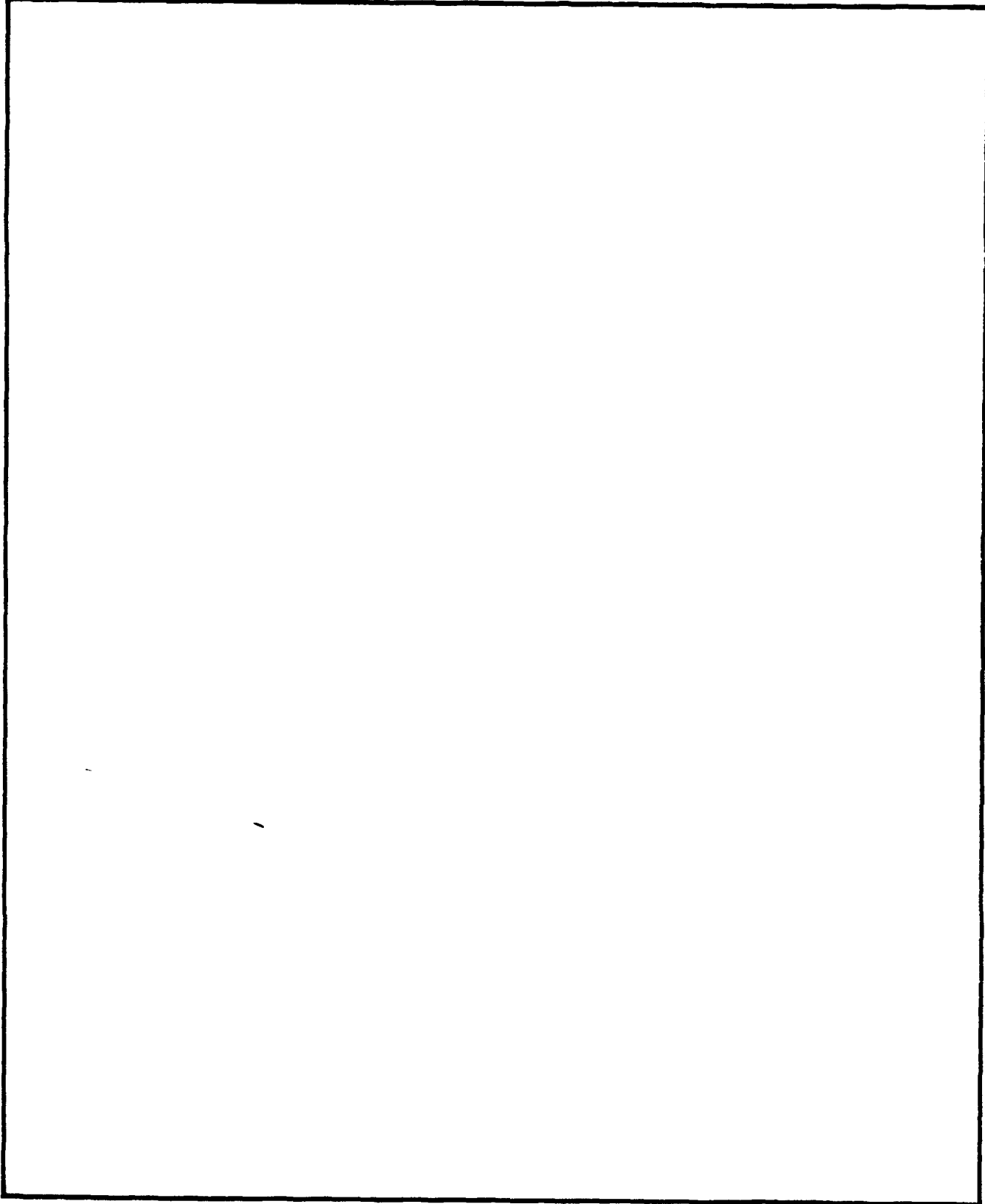
UNCLASSIFIED

SECURITY CLASSIFICATION OF THIS PAGE

REPORT DOCUMENTATION PAGE

1a. REPORT SECURITY CLASSIFICATION UNCLASSIFIED			1b. RESTRICTIVE MARKINGS	
2a. SECURITY CLASSIFICATION AUTHORITY N/A Since Unclassified			3. DISTRIBUTION/AVAILABILITY OF REPORT Approved for public release; distribution is unlimited.	
2b. DECLASSIFICATION/DOWNGRADING SCHEDULE N/A Since Unclassified				
4. PERFORMING ORGANIZATION REPORT NUMBER(S) Calapan Report No. 7170-A-5			5. MONITORING ORGANIZATION REPORT NUMBER(S) DNA-TR-86-306	
6a. NAME OF PERFORMING ORGANIZATION Calapan Advanced Tech. Center		6b. OFFICE SYMBOL (If applicable)	7a. NAME OF MONITORING ORGANIZATION Director Defense Nuclear Agency	
6c. ADDRESS (City, State, and ZIP Code) P. O. Box 400 Buffalo, NY 14225-0400			7b. ADDRESS (City, State, and ZIP Code) Washington, DC 20305-1000	
8a. NAME OF FUNDING/SPONSORING ORGANIZATION		8b. OFFICE SYMBOL (If applicable) SPAS/Adams	9. PROCUREMENT INSTRUMENT IDENTIFICATION NUMBER DNA 001-83-C-0182	
8c. ADDRESS (City, State, and ZIP Code)			10. SOURCE OF FUNDING NUMBERS	
			PROGRAM ELEMENT NO. 62715II	PROJECT NO. N99QMXA
			TASK NO. J	WORK UNIT ACCESSION NO. DH007300
11. TITLE (Include Security Classification) INTERPRETATION OF GAS TURBINE RESPONSE DUE TO DUST INGESTION				
12. PERSONAL AUTHOR(S) Batcho, Paul F.; Moller, James C.; Padova, Corso; and Dunn, Michael G.				
13a. TYPE OF REPORT Technical		13b. TIME COVERED FROM 850401 TO 860901	14. DATE OF REPORT (Year, Month, Day) 860901	
15. PAGE COUNT 84				
16. SUPPLEMENTARY NOTATION This work was sponsored by the Defense Nuclear Agency under RDT&E RMSS Code H342085466 N99QMXAJ00002 H2590D.				
17. COSATI CODES			18. SUBJECT TERMS (Continue on reverse if necessary and identify by block number)	
FIELD	GROUP	SUB-GROUP		
21	5		Performance Prediction J57 Turbojet	
18	3		TF33 Turbofan Dust Environment	
19. ABSTRACT (Continue on reverse if necessary and identify by block number) A measurements program currently underway at Arvin/Calapan Advanced Technology Center has been used in the evaluation of observed engine behavior during dust ingestion. The Pratt and Whitney TF33 turbofan and J57 turbojet were used in the investigation. Solid particle ingestion was found to erode the compressor blades and result in substantial performance deterioration. The engines were found to have increased susceptibility to surge at low power settings. The roles that anti-ice and intercompressor bleed air play in surge avoidance are discussed. A discussion of the fuel controller behavior in a deteriorated engine and its effect during steady state engine operation is also presented. Experimental data obtained during testing was compared to a predictive capability developed to describe deteriorated engine response. The effects of tip clearance, blade profile, and secondary flows were taken into account. The results show good agreement with experimentally observed engine behavior.				
20. DISTRIBUTION/AVAILABILITY OF ABSTRACT <input type="checkbox"/> UNCLASSIFIED/UNLIMITED <input checked="" type="checkbox"/> SAME AS RPT. <input type="checkbox"/> DTIC USERS			21. ABSTRACT SECURITY CLASSIFICATION UNCLASSIFIED	
22a. NAME OF RESPONSIBLE INDIVIDUAL SANDRA E. YOUNG			22b. TELEPHONE (Include Area Code) (202) 325-7024	22c. OFFICE SYMBOL DNA/CSTI

UNCLASSIFIED
SECURITY CLASSIFICATION OF THIS PAGE



SECURITY CLASSIFICATION OF THIS PAGE
UNCLASSIFIED

PREFACE

The work described in this report was performed by the Calspan Corporation under support of the Defense Nuclear Agency, Contract No. DNA001-83-C-0182. The work was performed during the period 1 April 1985 to 1 September 1986. The activity reported herein was conducted as part of a broad technology development program which is still in progress under the above contractual support by DNA.

The authors would like to thank the DNA technical monitor, Ronald M. Adams, for many helpful discussions during the course of the effort reported here.

CONVERSION TABLE

Conversion factors for U.S. Customary to metric (SI) units of measurement

MULTIPLY \longrightarrow BY \longrightarrow TO GET
TO GET \longleftarrow BY \longleftarrow DIVIDE

angstrom	1.000 000 X E -10	meters (m)
atmosphere (normal)	1 013 25 X E +2	kilo pascal (kPa)
bar	1 000 000 X E +2	kilo pascal (kPa)
barn	1 000 000 X E -28	meter ² (m ²)
British thermal unit (thermochemical)	1.054 350 X E +3	joule (J)
calorie (thermochemical)	4 184 000	joule (J)
cal (thermochemical)/cm ²	4 184 000 X E -2	mega joule/m ² (MJ/m ²)
curie	3 700 000 X E +1	giga becquerel (GBq)
degree (angle)	1 745 329 X E -2	radian (rad)
degree Fahrenheit	$^{\circ}\text{F} = (^{\circ}\text{C} + 459.67)/1.8$	degree kelvin (K)
electron volt	1.602 19 X E -19	joule (J)
erg	1.000 000 X E -7	joule (J)
erg/second	1.000 000 X E -7	watt (W)
foot	3.048 000 X E -1	meter (m)
foot-pound-force	1.355 818	joule (J)
gallon (U.S. liquid)	3.785 412 X E -3	meter ³ (m ³)
inch	2.540 000 X E -2	meter (m)
jerk	1 000 000 X E +9	joule (J)
joule/kilogram (J/kg) (radiation dose absorbed)	1.000 000	Gray (Gy)
kilotons	4 183	terajoules
kip (1000 lbf)	4 448 222 X E +3	newton (N)
kip/inch ² (ksi)	6 894 757 X E +3	kilo pascal (kPa)
knap	1.000 000 X E +2	newton-second/m ² (N-s/m ²)
micron	1 000 000 X E -6	meter (m)
mil	2.540 000 X E -5	meter (m)
mile (international)	1.609 344 X E +3	meter (m)
ounce	2 834 952 X E -2	kilogram (kg)
pound-force (lbf avoirdupois)	4.448 222	newton (N)
pound-force inch	1.129 848 X E -1	newton-meter (N-m)
pound-force/inch	1 751 268 X E +2	newton/meter (N/m)
pound-force/foot ²	4 788 026 X E -2	kilo pascal (kPa)
pound-force/inch ² (psi)	6 894 757	kilo pascal (kPa)
pound-mass (lbm avoirdupois)	4 535 924 X E -1	kilogram (kg)
pound-mass-foot ² (moment of inertia)	4.214 011 X E -2	kilogram-meter ² (kg-m ²)
pound-mass/foot ³	1 601 846 X E +1	kilogram/meter ³ (kg/m ³)
rad (radiation dose absorbed)	1.000 000 X E -2	*Gray (Gy)
roentgen	2.579 760 X E -4	coulomb/kilogram (C/kg)
shake	1 000 000 X E -8	second (s)
slug	1 459 390 X E +1	kilogram (kg)
torr (mm Hg, 0° C)	1.333 22 X E -1	kilo pascal (kPa)

*The becquerel (Bq) is the SI unit of radioactivity; 1 Bq = 1 event/s
**The Gray (Gy) is the SI unit of absorbed radiation.

TABLE OF CONTENTS

Section		Page
	PREFACE	iii
	CONVERSION TABLE	iv
	LIST OF ILLUSTRATIONS	vi
1	INTRODUCTION	1
2	BRIEF REVIEW OF EXPERIMENTAL APPARATUS AND OPERATION	3
	2.1 Test Cell	3
	2.2 Dust Injection System (DIS)	3
	2.3 Experimental Procedure	4
	2.4 Engine Description	5
	2.5 Observations	5
3	EROSION THEORY FUNDAMENTALS	7
4	FORMULATION OF PERFORMANCE DETERIORATION	15
	4.1 Tip Clearance Total Pressure Losses	16
	4.2 Modeling Blade Profile Losses	20
	4.3 Secondary Flow Losses	22
	4.4 Stage Performance Deterioration	24
5	MODELING COMPRESSOR RESPONSE	28
	5.1 Formulating an Averaged Stage Performance Map	28
	5.2 Generating an Eroded Compressor Map from Stage Stacking	29
	5.3 Effect of LPC and HPC Coupling	34
6	DETERIORATED ENGINE RESPONSE	39
	6.1 Bleed Air Controls	39
	6.2 Deterioration in Weight Flow	41
7	CONCLUSION	47
8	LIST OF REFERENCES	49
APPENDICES A	Development of Eroded Lift Coefficient	53
B	Approximate Potential Flow Solution for a Thin Highly Cambered Airflow	57
C	Derivation of Compressor Exit Properties	65
D	NOMENCLATURE	67

LIST OF ILLUSTRATIONS

Figure		Page
1	Erosion of 13th Stage Rotor Blade	17
2	Decrement of Efficiency Due to Tip Clearance Ratio Seven Axial Impellers	17
3	Blade Profile Erosion Near the Tip	19
4	Variation of Mean Camber Line with Erosion	19
5	Effect of Leading Edge Erosion on Cascade Lift Coefficient	23
6	Effect of Leading Edge Erosion on 2-D Loss Coefficient	23
7	Effect of Tip Clearance on Stage Performance	25
8	Estimate of Inlet Fluid Angle	25
9	Estimated Stage Performance Map from the 69.9 percent N2 Line	30
10	Estimated Stage Performance Deterioration from Measured Erosions	31
11	Computed Change in Compressor Performance	33
12	Illustration of Surge Margin Computation	33
13	Schematic of Numbering System for Matching Analysis	35
14	Low Pressure Compressor Matching Map	35
15	Low Pressure Turbine Matching Map	36
16	High Pressure Compressor Matching Map	36
17	Superposition of LPC and LPT Matching Maps; Deteriorated and Undeteriorated	38
18	Fuel Controller Map	42
19	Fourth Order Polynomial Fit to the Pre-Exposure Calibration Data	43
20	Deviation from Baseline Weight Flow vs. Rotational Speed Curve	44
21	Comparison of Predicted Deterioration with Experimental Data	46
22	Formulating Changes of the Mean Camber Line	54
23	Modified Thin Airfoil Theory	54

LIST OF ILLUSTRATIONS (Continued)

Figure		Page
24	Placement of the Vortex Sheet for Thin Airfoil Analysis	60
25	Determination of the Component of Freestream Velocity Normal to the Camber Line	60
26	Computational Results J57 Profile	61

LIST OF TABLES

Table		Page
1	Particle rebound characteristics	13
2	13th stage characteristics	26
3	Performance change due to erosion	26
4	Distribution of total pressure losses in the 13th stage	27
5	Computed performance loss in stages	27
6	Loss in compressor stability	34

SECTION 1

INTRODUCTION

Potential engine damage caused by the ingestion of dust-laden air is a serious consideration for the operation of gas turbine engines on unimproved runways or in dusty environments. Gas turbine engines are routinely tested for the effect of ingestion of solid particles according to the procedures of Military Specification MIL-E-5007D. However, the material used in MIL-E-5007D is basically crushed quartz at a very moderate concentration. This dusty environment is not appropriate to test for all realistic situations of potential engine damage. The reality of this issue has been dramatically emphasized by recent (1,2) incidents in which gas-turbine-powered air transports have attempted to traverse volcanic clouds. The material associated with the volcanic clouds and other dusty environments is more of an earth-like material, is often encountered at concentrations well in excess of those used in MIL-E-5007D tests, and has a particle size distribution different from MIL-E-5007D.

Several different mechanisms can be active in altering engine performance during or after exposure to a dust-laden environment. For most modern engines, the operating line is trimmed as close to the surge line as is possible. This operating line has a built-in margin for known degradation terms such as inlet distortion, transient gusts, and normal component wear. Encountering a particle laden environment of the type of interest here falls into the category of an unanticipated degradation and may be manifested in one or more of the following ways: (a) glassification of hot-section components, (b) erosion in compressor blading and rotor paths, (c) blockage of cooling paths, and (d) oil system or bleed air supply contamination.

If glassification occurs, it will likely take place on hot-section components of the machine. Whether or not it will happen depends upon many parameters, including engine operating point, the particular engine construction, and the physical and chemical properties of the dust cloud material. For the particular engines discussed in this report, glassification did not occur because the turbine inlet temperature was below that required for equilibrium melting of the material utilized.

Contamination of the bleed air systems was experienced during the measurements, but these results will not be discussed herein. The interested reader is

referred to other project reports (10-12). Severe compressor erosion was also experienced by all of the engines used in this measurement program and this particular aspect of the result will be described. The problem of component erosion by particulate-laden air flows has been the subject of study for many years (3-9) and is known to result in the loss of surge margin.

The discussion in this report will be confined to the effort expended in predicting the influence of erosion on the engine performance and in reconciling these predictions with the experimental data obtained from two TF33 turbofans and one J57 turbojet exposed to the same dust environment. One of the TF33 engines and the J57 engine that were exposed to the same dust mixture were completely disassembled so that detailed post-test measurements of the components could be obtained. As a result of the detailed measurements performed on the deteriorated engines and the operational experience obtained with them, it is possible to evaluate the predictive ability of a model developed in the following sections of this report.

SECTION 2

BRIEF REVIEW OF EXPERIMENTAL APPARATUS AND OPERATION

The TF33 turbofan and the J57 turbojet discussed in this report were operated in DNA's Large Engine Research Cell (LERC). The LERC is a test cell sized for high thrust large weight flow gas turbine engines and is described in detail in (10).

2.1 TEST CELL AND INSTRUMENTATION.

The engines were mounted in the LERC on an A/M-37T-6C test stand. The cell is an air-cooled noise suppression structure, composed of primary and secondary inlets, an augmentor tube, a perforated exhaust basket and an exhaust stack. The secondary inlet carries air entrained by the hot exhaust of the engine to the exhaust basket where it passes through perforations which break up the audible energy of the flow. The secondary inlet also serves to both cool the exhaust and to relieve the pumping load in the test chamber. It is relatively easy to create significant cell depression and ram effect biasing of engine thrust in a facility with only a primary inlet. However, because LERC has both primary and secondary air intakes it sustained a small cell depression of $\sim .03$ psig during operation of a TF33 at takeoff rated thrust.

The Control Cab is part of the A/M-37T-6C test stand which produced a sound proof environment for the engine operations. The Cab is equipped to provide all of the engine related readings that the pilot would see in the cockpit. The experiment was intentionally configured in this way in order to make the results as directly relevant to a pilot's viewpoint as possible (10).

The nearby control room contains readouts of cell and some engine parameters. The parameters which most directly indicate the engine's condition: EGT, N2, PT7, PLA, and bleed door position - are recorded on pencharts. A complete list of control cab parameters is also given in (10).

2.2 DUST INJECTION SYSTEM (DIS).

The DIS functions to deliver a continuous, spatially uniform concentration of dust to the engine face at velocities representative of the engine flying through a

quasi-stationary dust cloud. It is designed to deliver dust concentrations as high as 1000 mg/m³ having sizes up to 250 microns.

The DIS described in (10) consists of a compressed air supply, a weighbelt feeder, a feeder controller, a dust hopper, a set of venturis and nozzles, and an engine inlet tube. Dust falls from the hopper onto the belt of the feeder. The speed of the belt is adjusted by the controller to match the weight flow set point entered in the controller. The dust then falls from the belt and is carried by gravity and suction into a set of venturis through which air at high velocity is passing. The air conveys the dust through tubes to a set of nozzles at the intake plane of the engine inlet tube. The dust mixes with the initially clean intake air as it travels along the inlet tube until the spatial concentration of dust is uniform at the engine face. Previous use of similar hardware indicated a set of six nozzles located three engine inlet diameters upstream of the engine injection dust at the velocity of the clean intake air would provide sufficient mixing. Indeed it did; the intensity of the glow generated by the dust striking the moving fan blades varies with concentration and the glow intensity was uniform. The exit velocity of the dust is set by metering the pressure and flow rate of the conveying air upstream of the venturi. This was done by regulating the compressed air supply pressure and choking the flow upstream of the venturis.

2.3 EXPERIMENTAL PROCEDURE.

All engines were sent through a set of preliminary runs for the purposes of (a) training personnel in engine operation; (b) checking engine, instrumentation, and facility operation; and (c) generating pre-exposure engine baseline data. Following these runs, the engines were exposed to dust at concentrations, power settings, and exposure times given by their respective test matrices.

The test matrices were based on knowledge of previous engine behavior and environments the engines would be expected to experience. The individual runs were chosen (10-12) to give an indication of the influence of concentration and power setting on damage rate and damage mechanism.

Prior to each exposure run, dust weight flow was calculated to match the desired dust concentration. The volume flow of air was inferred through the use of a

nomograph of air weight flow versus power setting which was generated during the preliminary runs.

In each exposure run, the engine under test was brought to the EGT set point for the run, allowed to thermally stabilize, and then exposed to dust by first turning on the injecting air and then starting the weighbelt feeder. All parameters were recorded just before dust ingestion and several times each hour during ingestion.

Following each run, the last stage of both the high and low pressure compressors, the combustor, and the front and rear of the turbine were inspected by borescope for signs of exposure (e.g. erosion, glassification). The borescope was used most frequently to get a qualitative indication of the status of the tip clearance in the high pressure compressor because early in the testing it became apparent that surge due to clearance increases would be the dominant engine problem for the class of engines being used here.

2.4 ENGINE DESCRIPTION.

Results obtained from two engines, the P/W TF33-P11A and the P/W J57-P19W are described in this report. The J57 is a twin spool turbojet engine. At Takeoff Rated Thrust (TRT), it generates approximately 12,000 lbs of thrust while pumping 185 lbs/sec of air at a turbine inlet temperature of 1640°F. The TF33 is the turbofan derivative of the J57. It has one less low pressure compressor stage and one more low pressure turbine stage than the J57. The TF33 generates 18,000 lbs of thrust at MET, pumps 460 lbs/sec of air, and has a turbine inlet temperature of 1600°F. It is appropriate to run these engines as an erosion comparison pair because the two have very similar internal flow geometries and their HP compressor rotor blades are constructed from different materials; the HP compressor blades of the J57-P19W are steel and those of the TF33-P11A are titanium.

2.5 OBSERVATIONS.

Four engines have been run in the LERC in dust exposure tests: three TF33-P11As and one J57-P19W. Dust mixture, time at assigned power settings and concentration have varied among engines. However, after several hours of exposure,

the response of all engines has been a greater susceptibility to surge due to compressor erosion.

After nearly eleven cumulative hours of dust ingestion testing the first engine run in the LERC, a TF33-P11A, went from essentially steady state operation into a series of surges at a frequency of approximately one to two per second. The condition was relieved by retarding the throttle to idle. During the hour preceding the surges, the engine's exhaust temperature, pressure ratio, and fuel flow steadily dropped with respect to high pressure compressor speed. Approximately five minutes before the surges occurred, the engine began a slight autoacceleration; fuel flow, pressure ratio and temperature began to increase without any operator throttle movement. During the surges, the pressure ratio rapidly dropped and fluctuated in time with the surges and the exhaust gas temperature rose by over 300°F in ten seconds.

It is felt that this sequence of events occurred because of the inability of the eroded high pressure compressor to sustain the control set point pressure in the burner. The engine was operating in a regime in which compressor discharge pressure essentially equals burner pressure. The trend of the data just before surge suggests that the fuel controller increased fuel flow to bring the burner to its set pressure and eventually created enough backpressure on the compressor to surge it. If the engine had been operating at a higher power setting, then the events likely would not have occurred because compressor discharge pressure would have been greater than burner pressure and surges would have occurred only when trying to accelerate through or operate in the range in which burner and compressor discharge pressures are essentially equal.

Severe compressor erosion accompanied by hard engine surges describes the behaviors of the second and third TF33 and the one J57. Both were brought into states of substantial deterioration at higher power settings and only while attempting to accelerate from idle did surge occur. In states of relatively mild deterioration, acceleration rate had to be limited and after heavy deterioration, the engines could not be accelerated at all. It also became apparent with these engines that over the course of exposure, the erosion caused a readjustment of operating parameters; especially rotor speeds and fuel and air flows. References (10-12) contain a complete description of the observed engine behavior as a function of dust exposure.

SECTION 3

EROSION THEORY FUNDAMENTALS

Engine components which are exposed to dust laden air sustain damage by continuous pitting and cutting of the metal surfaces. Impact velocities of the particles are influenced by inlet air velocity and rotational speed of the rotor blades. Typically, the impact velocity at the first engine rotor is 600 ft/s or less. After the first impact, a dust particle—or fragments of it—will rebound, may accelerate or decelerate as it experiences drag in the air, may collide with other particles, and then impact again on moving or stationary engine surfaces.

At the microscopic level, a statistical approach must be used in describing the erosion process because the simple conceptual case of a single particle impacting at a given velocity and angle is in practice "randomized" by several complicating factors. For example, the particles themselves are inhomogeneous in hardness and irregular in shape with several sharp corners. As they approach the metal surface with no preferential orientation, they do a random amount of work on it. The work will vary from very little—for example for impact broadside on a flat surface—to transfer of a substantial fraction of the particle momentum into deformation of target material or shear and impulse of target fragments. In addition, the effective angle of impact is randomized by the fact that, after an initial incubation period, the target material becomes pitted with craters and the local impact angle between the small particle and the eroded surface may deviate considerably from the approach angle before the impact. Furthermore, the particle velocity may be randomized due to particle-particle collisions, at least above some low level of dust concentration. All these effects have been discussed previously in the literature (13-17).

A methodology to predict erosion of gas turbine components must separately define the particulate environment from front to rear of the engine, the shape of the target area and the associated flowfield, and the erosion rate for the special target materials. Although in an engine the shape of the target surfaces is very complex, it is in fact the best known—at least initially—among the above factors. The flowfield for the uneroded engine is also complex, but known, since the effect of the presence of the particles on the aerodynamics of the engine can be ignored (to a first approximation for all the low-concentration applications of interest here). On the other hand, local

changes in geometry may become very important in accelerating or decelerating locally the instantaneous erosion rate as the engine components are eroded.

Among the fundamental parameters for modeling erosion, the erosion rate is conceptually well defined and may be obtained experimentally (18). The erosion rate is determined by measuring the weight of a target specimen before and after testing. It is expressed as milligrams of material removed per gram of impinging solid particles. For the metallic materials of interest in engines, a considerable body of experimental data exists. However, its interpretation is not always clear because of experimental differences in the ways the data were obtained and the still inadequate development of erosion theory. For example, for a gas-particle jet impinging on a target, the amount of impinging solid particles is known from the particulate feed rate and the exposure time. For a target immersed in a gas particle stream a capture ratio must be determined. This is the case for the moving or stationary parts of an engine for which the cumulative mass of dust ingested is given by:

$$L = (\text{particle concentration}) \times (\text{rate of volumetric flow}) \times (\text{exposure time})$$

where all quantities are taken at the engine inlet. The difficulty in determining appropriate values of the capture ratio at specific engine locations for stator vanes, rotor blades and housing surfaces will become apparent from the later discussion of gas-particle dynamics in multistage turbomachines.

Limiting considerations to well-defined erosion rate data, one finds that some major trends are well established and bear significantly on the gas turbine erosion problem. Experimental observations (16, 18, 19, 20) indicate that dust angle of attack and velocity strongly influence the erosion rate for a given combination of dust and target material. Other parameters such as particle size and shape, and dust concentration may have a lesser effect, if any, on the results.

The influence of angle of attack on the removal rate of material is one of the most distinct features of the erosion of ductile materials such as engine metals. In the velocity range from 250 to 600 ft/s, the erosion rate increases rapidly with angle of attack from zero at 0° to a maximum value which occurs at an angle of approximately 20° . As the angle of attack increases further from this value, the erosion rate decreases gradually to a residual value at 90° . A relationship of the erosion rate to the dust

velocity based on the supposition that the erosion process be proportional to the kinetic energy of the oncoming particles was proposed in early investigations. However, there is a lack of agreement among the results of the theories based on kinetic energy exchange and the experimental results. This is still a perplexing issue in the field of solid particle erosion. The conventional expression for volume removal - volume removed per particle impact - is given as

$$\varepsilon = g v_p^a (r_p)^b f(\alpha_p) \quad (1)$$

where g is a functional representing the dependence on all of the parameters not explicitly stated and,

v_p is the particle impact velocity

r_p is the mean radius of the impacting particle

$f(\alpha_p)$ is the function of the dust angle of approach (discussed above)

a is the velocity exponent

b is the particle size exponent

The velocity exponent* has been generally found to range from two to three for materials displaying ductile behavior and a wide range of particle impact conditions; however, exponents up to four have been proposed (6). Note that an even larger variation of the velocity exponents is reported in the literature for brittle materials with values that range from 1 to 6.5 (21).

Less is known about the particle size exponent. For metals, it is generally stated that the volume removal is independent of particle size for particle diameters in excess of 100 μm (16). However, for the smaller particle sizes which are of interest in turbomachinery applications, the variations in particle size effects may be significant. For example, in brittle materials tested with particles as small as 8 μm , the particle size exponent was found to vary from 3 to larger than 4, and it was found to be coupled with the velocity exponent as well (20).

Erosion in multistage turbomachines is significantly more complex than the erosion of simple targets such as flat or cylindrical specimens. This is due primarily to the changes which the erodent particles incur from the inlet to the exit of the engine as well as the difficulties in tracing the particle trajectories through the engine

gas path after multiple impacts. It is also clear that the cumulative influence of particle dynamics and changes in the dust environment makes erosion of both stationary and moving machine components very dependent on their stage location and on the specific engine design.

The motion of the particles which are convected through the compressor and the turbine should be analyzed to derive bounds on the location and severity of component erosion. Considerations related to the trajectories for particles having different sizes are necessary; (a) to estimate the erodent weight and characteristics at each stage location and (b) to estimate heat-transfer levels while the particles travel through the combustor to the turbine stages.

Particles suspended in a gas flow move under the influence of forces exerted on them by the gas. Ordinarily, the reaction of these forces affects the gas flow only to a negligible extent but this influence may have to be considered at high concentration or for highly turbulent flows. More importantly for the engine application, the interaction of particles with wakes of other particles may be of consequence. The equation of motion of individual particles equate the product of mass and acceleration to the sum of various forces; namely, viscous drag, gas pressure gradient (or alternatively gas acceleration), apparent mass acceleration, and Basset force. The latter force accounts for deviation of the flow pattern around the particle from that of steady flow. In addition, lateral forces on the particles may develop as a result of particle rotation, slip in the shear flow of a boundary layer, and other effects. Fortunately, the 200:1 ratio between the density of the particulate and the density of the gas can be used to simplify the analysis in the application of interest here. With such a high density ratio, it can be shown that it is reasonably justified to equate the mass-acceleration term to the viscous drag only. Because the flow in gas turbines is severely swirled, residual effects from other forces cannot be ruled out entirely and the conclusions derived here are contingent upon experimental verification.

In the approximate form, the equation of motion for a spherical particle convected by the gas becomes:

$$\frac{\pi D_p^3}{6} \rho_p \frac{d\vec{u}_p}{dt} = \frac{C_d \pi D_p^2}{4} \cdot \frac{\nu}{2} |\vec{u} - \vec{u}_p| (\vec{u} - \vec{u}_p) \quad (2)$$

where the substantial derivative D/Dt is taken along the path of the particle and

$$\begin{aligned} D_p &= \text{diameter of particle} \\ \bar{u}_p &= \text{velocity of particle} \\ \bar{u} &= \text{velocity of gas} \\ \rho, \rho_p &= \text{gas and dust densities} \end{aligned}$$

The Reynolds number for a particle can be expressed as

$$Re_p = \frac{\rho D_p |\bar{u} - \bar{u}_p|}{\mu} \quad (3)$$

In our application, we estimate

	Compressor (front)	Compressor (rear)	Combustor	Turbine (front)	Turbine (rear)	Units ()
ρ	$= 0.07 - 0.3$	$0.3 - 0.5$	0.5	$0.25 - 1.5$	$0.15 - 0.03$	lbm/ft^3
$\mu \times 10^7$	$= 3.6 - 5.4$	$5.4 - 6.8$	$6.8 - 12$	$12 - 9$	7	$\text{slugs}^{-1}\text{ft}^{-1}$
$ \bar{u} - \bar{u}_p $	$= 0-560$	$0-600$	$0-80$	$0-1030$	$0-830$	ft/s
D_p	$= 1-800$	$1-30$	$1-30$	$1-30$	$1-30$	μm

and consequently

$$Re_p = 0 \text{ to } 2300$$

For this range, the relationship for the particle drag coefficient can be given as

$$C_d = \frac{24 (1 + 1/6 Re_p^{2/3})}{Re_p} \quad (4)$$

which fits the standard drag curve to better than 30% and the trajectory of particles could be calculated for any known airflow pattern and given particle size.

A useful parameter which indicates how an initial velocity difference $u - u_p$ decays in time in a constant gas velocity is easily derived from Eq. (3). For Re_p

less than 100 where $C_d = \frac{24}{Re_p}$ to a good approximation, it can be shown that an initial velocity difference $(u - u_p)$ decays exponentially with a relaxation time τ_v given by

$$\tau_v = \frac{D_p^2 \rho_p}{18 \mu}$$

For larger Re_p values, τ_v remains a convenient qualitative measure of velocity relaxation. For the present application, it is estimated that in the cooler (lower viscosity) gas situation, the relaxation times are in the range:

$$\begin{aligned} (\tau_v)_1 &= 0.03 \text{ ms for particles } 1 \text{ } \mu\text{m in diameter} \\ (\tau_v)_{30} &= 0.5 \text{ ms for particles } 30 \text{ } \mu\text{m in diameter} \end{aligned}$$

The above relaxation times may be compared with the time required for a blade to transit a vane exit passage in order to determine approximately how many times a particle is likely to strike the same rotor blade and where the impacts are more likely to occur. However, a description of how the particles will rebound upon impact is needed first.

Particle rebound correlations were obtained by Tabakoff (22) using an experimental approach based on Laser Doppler Velocimeter (LDV) measurements. A large number of impacts of fly ash particles having a diameter of $15 \text{ } \mu\text{m}$ were observed as they impinged on metal targets at 320 ft/s. Targets of annealed 2024 aluminum, 6Al-4V titanium and 410 stainless steel were used. From the measurements, values of the average velocity restitution ratio (V_2/V_1) and the average directional coefficient (β_2/β_1) were obtained for impingement angles from 15 to 75° . The shape of the statistical distributions of the above parameters were also reported because they are important for detailed trajectory calculations.

The velocity restitution ratio parameter is a measure of the momentum lost by the particle at impact and as such it should correlate with the work done on the target material. This work, in turn, determines the erosion rate. In (22) it is shown that the normal velocity restitution ratio V_{N2}/V_{N1} and the tangential restriction ratio V_{T2}/V_{T1} do not contribute equally to ductile erosion. In fact, the average value of the tangential velocity restitution ratio is the only parameter which supports the

theory that erosion is proportional to a particle momentum loss at impact. This is because the maximum erosion of the metallic materials tested occurs at values of the impingement angle where the tangential velocity restitution ratio is low. For our purpose the generic values of Table 1 were used.

Table 1. Particle rebound characteristics.

β_1	=	0	20	45	70°
V_{T2}/V_{T1}	=	1	0.7	0.7	1.3
V_{N2}/V_{N1}	=	1	0.5	0.4	0.3

It should be noted that the effect of approach velocity on the mean value of the restitution ratios has been neglected in accordance with the assumptions and findings of several authors (23, 24).

Using the above particle rebound characteristics and the relaxation times computed earlier, the frequency and location of impacts of a particular particle on a given rotor blade were estimated. At each stage it was assumed that all the particles initially impact the rotor near the leading edge. The results of this very simple analysis indicate that nearly all of the particles will strike the same rotor blade twice. A small fraction of the particles could strike the blade three times. The blade leading edge and trailing edge regions experience the highest number of impacts. The trend indicated by the comparison of 30 μm particles to 1 μm particles is that erosion of the stationary blades will decrease and erosion of the rotating blades will increase if the finer particles are more abundant. In general, a less severe erosion is indicated in the hot turbine flow where the velocity relaxation times are considerably smaller.

In (6) and (25), detailed predictions of particle trajectories, erosion patterns and eroded mass are discussed. The results were obtained using a sophisticated Monte Carlo simulation model of the erosion process in relatively simple gas turbine cascades. A one and one-half stage compressor and a two stage turbine case were considered. In principle, detailed descriptions of erosion intensity and pattern can be obtained a priori for stationary and moving gas turbine components by using that technique. However, at the present time the model does not include modeling of particle fragmentation nor does it account for erosion rates at elevated temperatures.

From the above discussion it is clear that a number of fundamental erosion issues must be resolved before reliable a priori predictions of erosion in realistic turbomachine configurations can be made. At present the two most important areas for which basic information is lacking are (a) particle breakup models and data and (b) erosion rates at elevated temperatures.

Having recognized this situation, the remainder of this study followed the approach of a semiempirical analysis in which experimental observations relative to the level and pattern of erosion in the TF33 and J57 engines were utilized to interpret the operation of the deteriorated engines. These observations could also be used to guide in the prediction of deteriorated engine behavior for different engine types which may be tested in the future.

SECTION 4

FORMULATION OF PERFORMANCE DETERIORATION

Ingestion of dust-laden air has the effect of deteriorating the performance of a gas turbine engine as a result of gas path component erosion. This erosion changes the structural character and thus the aeroelastic behavior of the engine as well as the aerodynamic performance. The unsteady aeroelastic stability is not expected to be rapidly influenced by erosion. However, the eroded blades are known to quickly lose the ability to efficiently increase the total pressure of the stage. In an effort to quantify the loss in performance of the engine, a compressor stage will be discussed and then extrapolated into a complete compressor map. First a suitable stage performance map will be calculated from the pre-ingestion compressor map. Then, a deteriorated stage performance will be determined from loss correlations and measured blade erosion. The deteriorated stage performance maps are finally stacked to arrive at an overall deteriorated compressor map.

To estimate the change in stage performance with respect to erosion, the primary sources of total pressure loss affected by the blade aerodynamic efficiency were considered. Attention was given to three distinct origins of total pressure loss: (a) losses associated with increasing tip clearance; (b) profile losses due to the blade boundary layer; and (c) secondary flow losses produced at the hub end wall and casing boundary layer regions. Of considerable interest is the presence of total pressure losses in the tip region which are large in comparison with the other regions. Within the compressor, the impact of dust-laden air will cause considerably greater blade leading edge erosion at the larger span locations as well as tip region erosion. This blade profile modification is illustrated in Figure 1 which illustrates a J57 HP compressor blade that has been subjected to a dusty environment (11). This machine uses both an LP and a HP compressor and the erosion of both components is described in (11). It suffices here to note that the severity of erosion increases from the front to back stages of both compressors, being most severe in the seven stage HP compressor. A region of significant erosion will cause a total pressure distortion in the radial direction (26). This effect leads to a flow instability that could cause boundary-layer separation in the tip region. Such behavior will degrade the stage performance and may lead to a compressor surge.

Several authors (26-32) have presented techniques for estimating losses due to tip clearance leakage. Experimental results (27) show a linear decrease in efficiency, with increased tip clearance to blade height ratio, Figure 2. Theoretical models have shown fair agreement (29) with experimental results in certain regions of clearance ratio.

Recently a model presented in (27) was found to agree well with the experimental result of seven different axial flow compressors (see Figure 2). The model accounts for leakage loss and pressure gradient losses associated with the flow interaction of the leakage vortex. The suggested expression given in (27) for changes in efficiency in an axial flow compressor blade row is given in equation 5.

$$\frac{\Delta \eta}{\lambda} = \frac{.759}{\bar{r}/r_t} \frac{s \phi \psi \sigma}{c \sin^3 \beta_m} + \frac{1.17 \phi}{\sigma^2 \bar{r}/r_t \tan \beta_m} \quad (5)$$

where $\sigma = 1 - .3 \lambda$

$\lambda = \text{tip clearance } (\tau) / \text{blade height } (h)$

$$\eta_{st} = 1 - \frac{(\Delta P_t)_L}{(\Delta P_t)_{is.}} = 1 - \frac{\xi}{\psi_{is}}$$

$\bar{r}/r_t = \text{hub-tip mean radius } (\bar{r}) / \text{tip radius } (r_t)$

The variables used in equation 5 are local values at the blade tip. Figure 3 illustrates the substantial change in chord and thickness experienced in the tip region of the 16th stage HP compressor blade of the J57 machine (11). The marked erosion at the leading edge may have a substantial influence on the pressure distribution on the blade surface and thus result in a decrease in the strength of the leakage vortex. For this reason, equation 4 is expressed in terms of cascade lift coefficient which will then be modeled for changes in leading edge erosion. The definition of cascade lift coefficient based on mean velocity is given in equation 6.

$$C_L = \frac{\psi}{\phi} \frac{s}{c} \cos \beta_m \quad (6)$$

where ψ is pressure coefficient

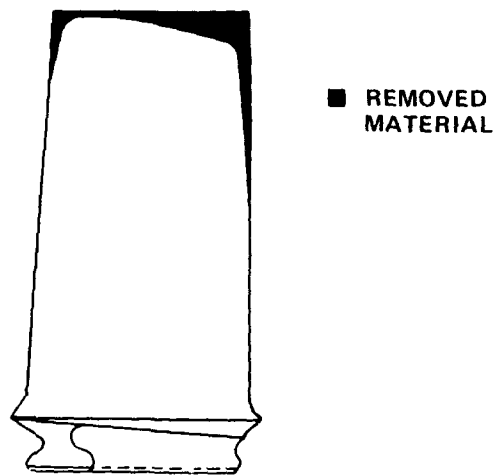


Figure 1. Erosion of 13th stage rotor blade.

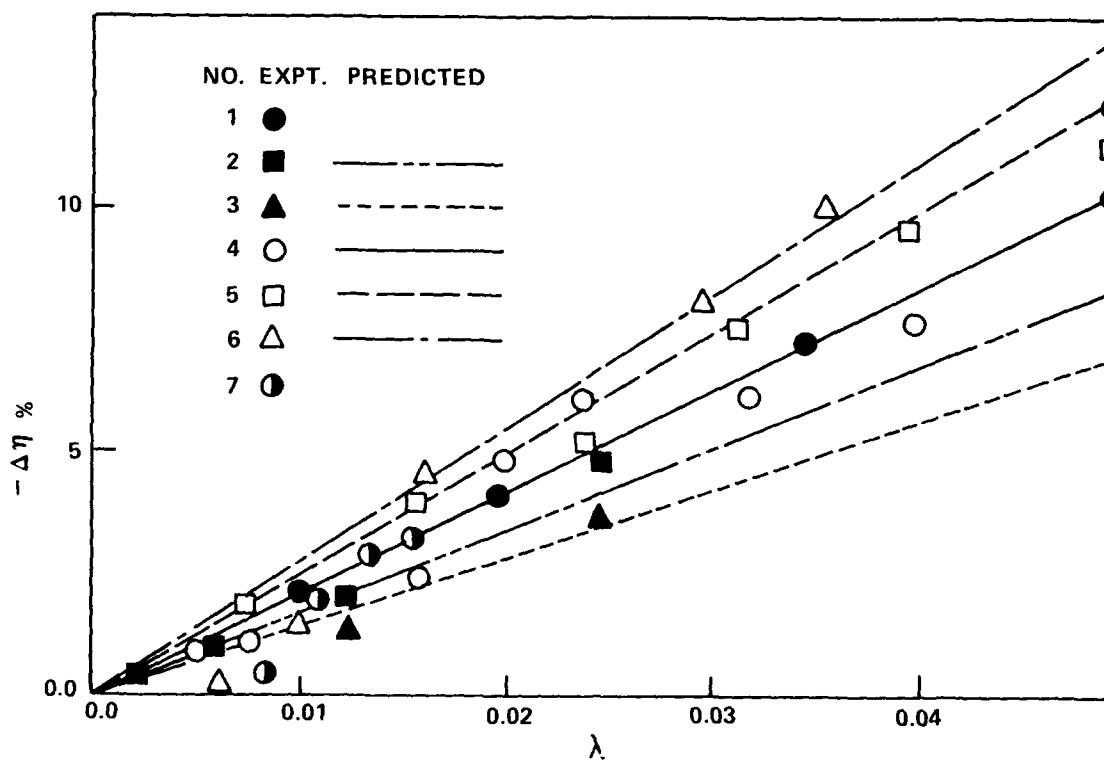


Figure 2. Decrement of efficiency due to tip clearance ratio seven axial impellers.
(Taken from [1].)

ϕ is flow coefficient
 s/c is solidity at the midspan
 β_m is the mean fluid angle at midspan

$$\epsilon_{tip} = \left[\frac{.759}{\bar{r}/r_t} \sqrt{\frac{\phi^2 \sigma C_L}{\sin^3 \beta_m \cos \beta_m}} + \frac{1.17 \phi}{\sigma^2 \bar{r}/r_t \tan \beta_m} \right] \psi \lambda \quad (7)$$

The definition of efficiency is substituted to obtain an expression for the total pressure loss coefficient due to tip clearance effects. Equation 7 can be used to estimate the total pressure loss induced by increased tip clearance and by changes in the lift coefficient resulting from blade profile changes at the tip.

As illustrated earlier, the principal effects of erosion on the airfoil are removal of material in the pressure surface leading edge region, thinning of the trailing edge, and reduced leading edge radius. Reference 7 shows a significant increase in two dimensional profile losses as a result of blade erosion. Due to the high loading at the leading edge of an airfoil, it is expected that any change in this region will be significant. The effect of thickness distribution along the airfoil was assumed to have a minor effect on the overall aerodynamic performance of the airfoil. The effect of leading edge erosion will be modeled by a change in the mean camber line of the airfoil (see Figure 4). This change will result in an increase in the angle of zero lift and thus a decrease in blade lift coefficient at fixed inlet flow angle. A reasonable estimate of the contribution to the lift coefficient from the mean camber line is accomplished using thin airfoil theory. It is demonstrated in Appendix A that for any given eroded state,

$$\Delta C_l = 1.5 \pi E (\Delta c) \quad (8)$$

Equation 8 approximates the change in two dimensional blade lift coefficient due to leading edge erosion and is dependent on the height of the uneroded camber line at the eroded leading edge. Note that the change in blade lift coefficient from equation 8 should be subtracted from the uneroded blade lift coefficient when used to estimate profile losses. For the purpose of this report, the uneroded blade lift coefficient is obtained by a method outlined in the following paragraph.

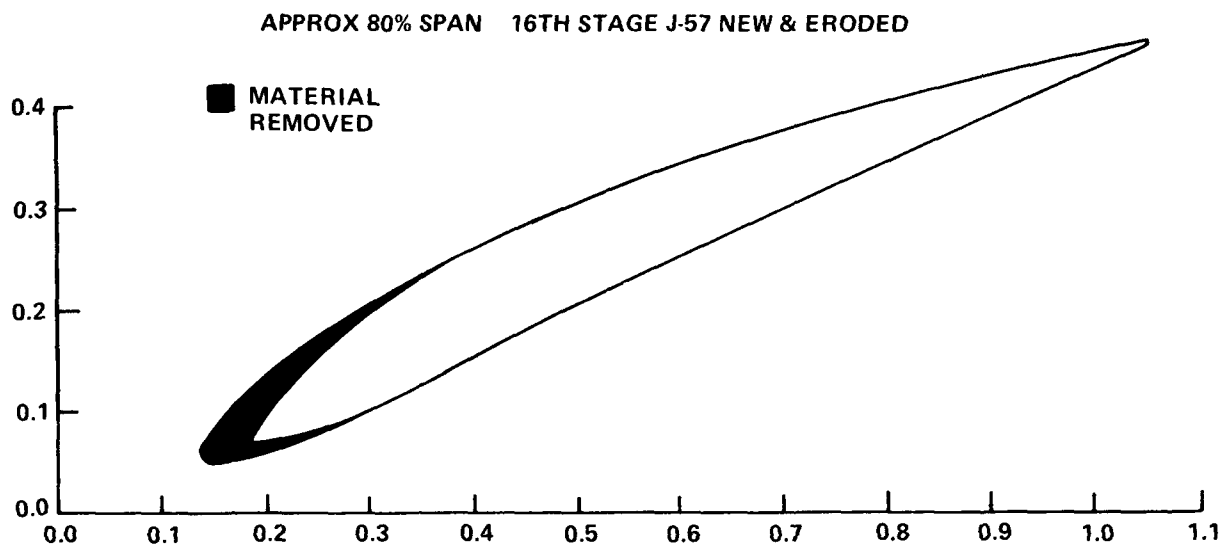


Figure 3. Blade profile erosion near the tip.

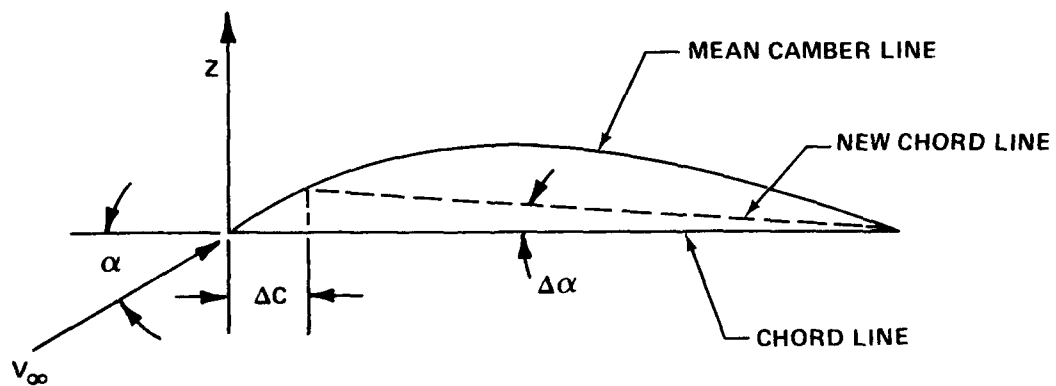


Figure 4. Variation of mean camber line with erosion.

It is not recommended that classical thin airfoil theory be used to find the uneroded blade lift coefficient since turbomachinery blades are typically highly cambered. Rather, an improved potential flow solution was obtained by using a modification of classical airfoil theory which removes the assumptions of small angle of attack and small camber angle. The method used in this development is given in Appendix B and does not require extensive computational facilities. The result for the J57 profile is given below.

$$C_{\ell} = 4.724 \sin \alpha + 1.614 \cos \alpha \quad (9)$$

4.2 MODELING BLADE PROFILE LOSSES.

Thus far the development has concentrated on the tip region. The considerations made in deriving the local C_{ℓ} apply also to any other spanwise location. In order to relate the blade lift coefficient to the cascade lift coefficient, a modifying coefficient (described in (34) and (35)), K , must be used to account for the effects of channel flow in the cascade. Although the use of a cascade coefficient may seem to oversimplify the formulation of the cascade lift coefficient, it has been found to be reasonable in subsonic flow (34,35). Typical values of K are approximately 0.5 for axial flow compressors. For small changes in chord, K can be assumed to remain constant.

Now that a means of tracing changes in cascade lift coefficient with respect to leading edge erosion exists, a method of relating lift coefficient to cascade profile losses must be developed. From a two-dimensional control volume analysis on a cascade, expressions for lift and drag coefficients have been formulated (36) and are given below.

$$C_D = \frac{(\Delta P_t)_L}{1/2 \rho w_m^2} \frac{s}{c} \cos \beta_m \quad (10)$$

$$C_L = 2 \frac{s}{c} \cos \beta_m (\tan \beta_i - \tan \beta_{ii}) - C_D \tan \beta_m \quad (11)$$

The loss coefficient based on mean velocity is given by the total pressure loss across the blade divided by the dynamic pressure.

$$\xi_m = \frac{(\Delta P_t)_L}{1/2 \rho w_m^2} \quad (12)$$

Equation 11 was developed from a two dimensional analysis and may be solved for drag coefficient to arrive at a two-dimensional profile loss coefficient with the use of equations 11 and 12. To express loss coefficient with respect to tip rotational speed, an assumption of constant axial velocity through the blade row is made to yield equation 13.

$$\xi_m \phi^2 \cos \beta_m = \xi \quad (13)$$

$$\xi_{PROFILE} = \phi^2 \cos^2 \beta_m \left[\frac{2(\tan \beta_i - \tan \beta_{ii})}{\tan \beta_m} - \frac{c}{s} \frac{C_L}{\sin \beta_m} \right] \quad (14)$$

There are numerous detailed accounts of two-dimensional cascade tests which will give a good estimate of the profile losses (37). With the stage performance map given and the blade lift coefficient computed, where $\alpha = \beta_i - \nu$, the modifying coefficient may be obtained using equation 5.

In addition, from knowledge of uneroded lift coefficient, profile loss coefficient, and blade row geometry the $\tan \beta_i - \tan \beta_{ii}$ term may be computed. The blade profile of a J57 16th stage compressor blade was substituted into equations A-9 and A-4 to yield changes in lift and total pressure loss coefficient with respect to

leading edge erosion. (see Figures 5 and 6). Since erosion is concentrated in the tip region, the integrated profile loss increase is not represented by Figure 6. Equation 15 accounts for the uneroded portion of the blade near the hub and provides the averaged total pressure loss coefficient due to leading edge erosion in the tip region.

$$\xi_{\text{PROFILE}} = \xi_o \left[\omega_e (\xi / \xi_o - 1) + 1 \right] \quad (15)$$

where

ω_e = fraction of blade height influenced

4.3 SECONDARY FLOW LOSSES.

The losses due to secondary flows must also be examined due to their strong dependence on lift coefficient. The literature contains correlations (e.g. 34) of losses due to secondary flows given by $C_D = .018 C_L^2$ or referring to equations 9 and 13 a loss coefficient given by equation 14.

$$\xi_{\text{sec}} = .018 \phi^2 C_L^2 c/s \cos \beta_m \quad (16)$$

Since the secondary flow is the result of the hub endwall and casing boundary layers and their respective local lift coefficients, equation 16 will be separated into two parts. The correlation will be assumed to have equal contributions from endwall and casing boundary layers for the uneroded condition. As the tip region erodes the local two dimensional lift coefficient will decrease and thus secondary flow losses in the tip region decrease. The contribution due to the hub endwall region will be assumed constant due to relatively little erosion in this region. The new expression for secondary flow losses is given in equation 17 and may be calculated from the previous formulation of lift coefficient.

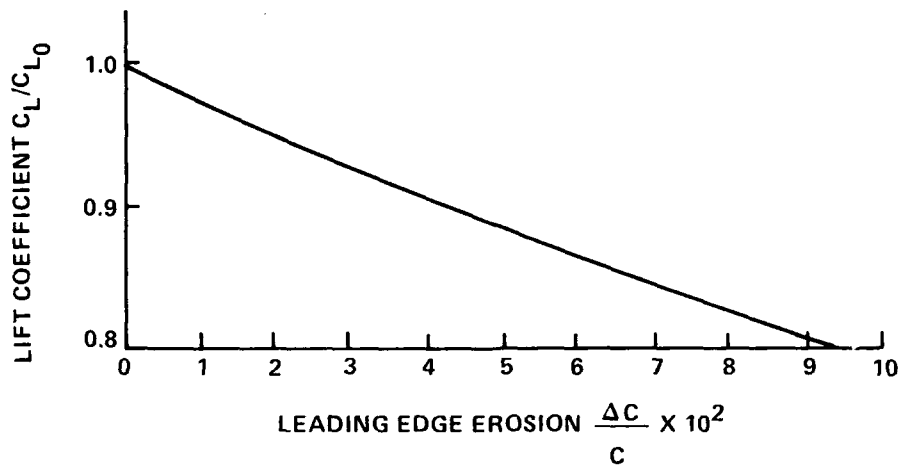


Figure 5. Effect of leading edge erosion on cascade lift coefficient.

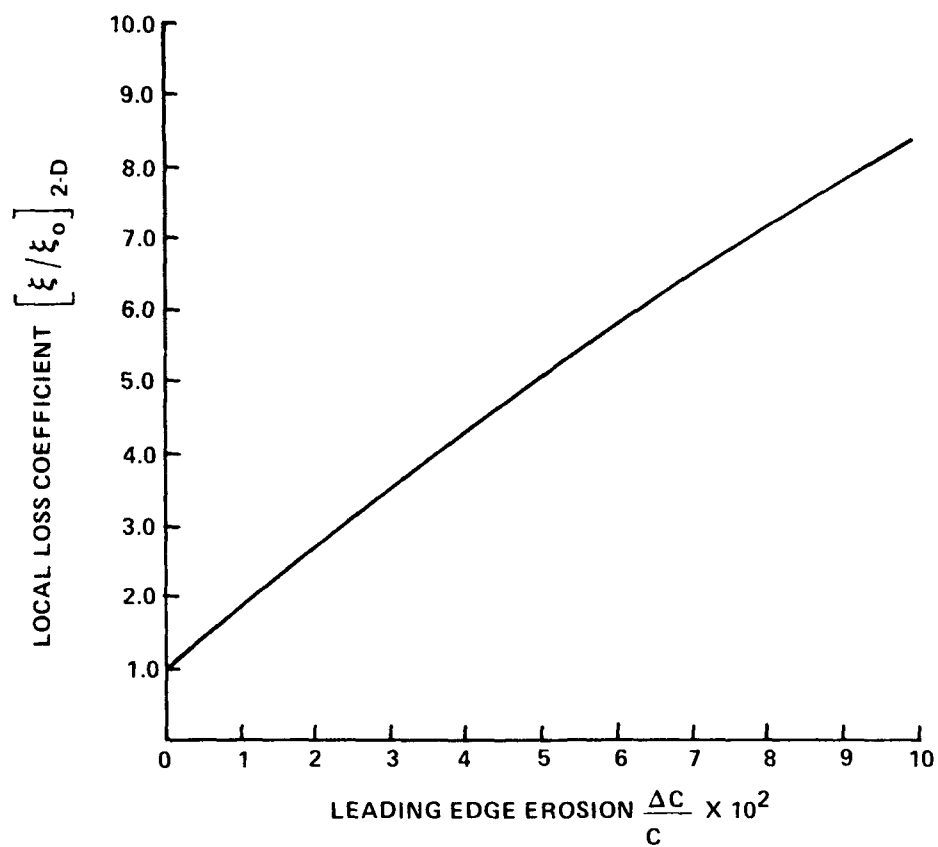


Figure 6. Effect of leading edge erosion on 2-D loss coefficient.

$$\xi_{\text{sec}} = .009 \phi^2 \cos \beta_m \left[\frac{c_t}{s} C_{L_t}^2 + \frac{c}{s} C_{L_{\text{HUB}}}^2 \right] \quad (17)$$

4.4 STAGE PERFORMANCE DETERIORATION.

In order to study the effect of erosion on overall compressor deterioration, a loss in stage performance will be modeled. Experimental studies presented by (26) show the effect of tip leakage flow on a stage performance map (Figure 7). The study indicates that a change in slope does not occur, but rather an overall shift of the pressure coefficient and efficiency versus flow coefficient curves produces the observed result. This behavior will allow the changes in performance to be modeled at the design point and then used to produce an entire eroded performance map. This assumption is of particular importance since the modeling results are not expected to yield accurate predictions at off design operating points. To estimate efficiency and performance, the previous total pressure loss formulations will be used with the knowledge of the stage characteristics. Therefore, stage to stage fluid angle must be known. If the stage flow characteristics are not available, as is the case for many older engines, an estimate of fluid angles must be made from a given stage performance map. Compressor stages are typically designed to have approximately a fifty percent stage reaction for peak efficiency. The flow coefficient may be related to the relative mean fluid angle by equation 18.

$$\phi = 1/2 \cot \beta_m \quad (18)$$

The design point is taken to be at a constant flow coefficient as the stage deteriorates. On this basis, the mean fluid angle and difference in tangents of inlet and exit fluid angles will be assumed constant at the design point. The assumption of fifty percent stage reaction also gives an equal amount of losses through rotors and stators. The computed and measured stage characteristics are given in Table 2 for the 13th stage of the J57 HP compressor.

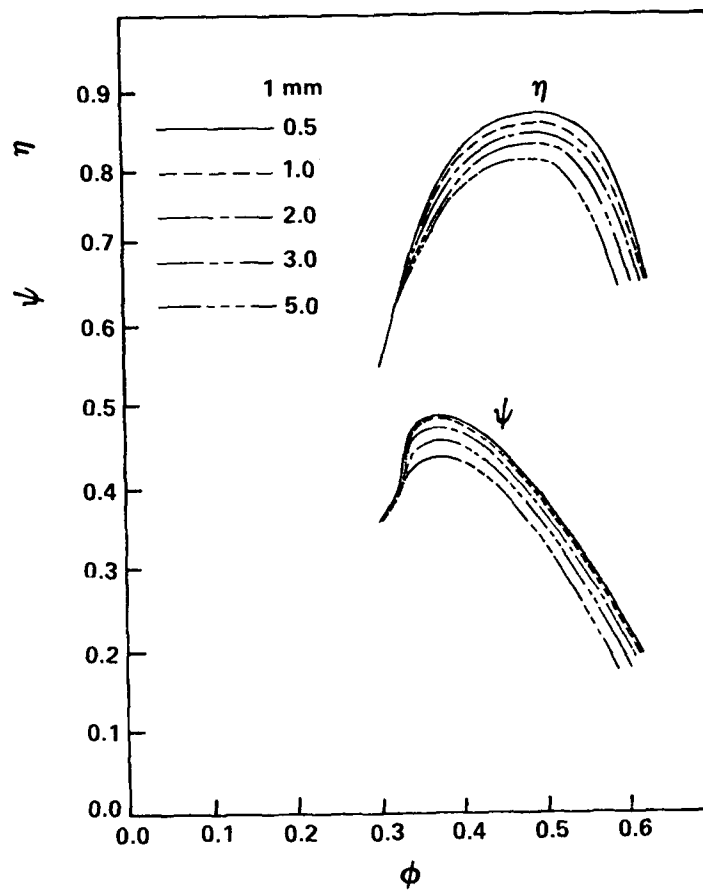


Figure 7. Effect of tip clearance on stage performance.
(Taken from [2].)

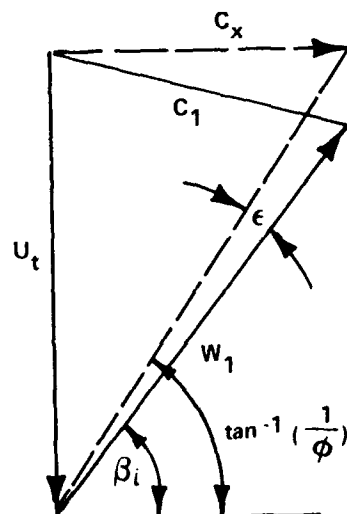


Figure 8. Estimate of inlet fluid angle.

Table 2. 13th stage characteristics.

mean to tip radius	\bar{r}/r_t	0.92
solidity	c/s	1.0
design flow coefficient	ϕ	0.685
design pressure coefficient	ψ	0.543
tip clearance	τ	0.05"
blade height	h	2"
mean fluid angle	β_m	36°
	$\tan \beta_i - \tan \beta_{ii}$	0.464
stagger angle	ν	30°
polytropic efficiency	η_{pc}	0.86
profile loss coefficient	$\xi_{profile}$	0.012
cascade modifying coefficient	K	0.20
cascade lift coefficient	C_L	0.64
total loss coefficient	ξ	0.050

To estimate the inlet relative fluid angle, and thus angle of attack to be used in equation 18, a typical velocity triangle at the inlet was constructed (Figure 8). Equation 19 was used to estimate the inlet fluid angle.

$$\beta_i = \tan^{-1} (1/\phi) - \epsilon \quad (19)$$

where $\epsilon \approx 5^\circ$

The measured blade erosion and calculated changes in pressure coefficient and efficiency at the design point are given in Table 3 for the 13th stage.

Table 3. Performance change due to erosion, 13th stage.

chord change at tip	$\frac{\Delta c}{c}_{tc}$	0.06
average chord change	$\Delta c/c$	0.03
leading edge influence	ω_e	0.3
decrease in efficiency	$\Delta \eta_{st}$	0.064
decrease in pressure coefficient	$\Delta \psi$	0.041
tip clearance increase	$\Delta \tau$	0.05"
increase in loss coefficient	ξ/ξ_0	1.39

The above calculations were made assuming no increases in losses through the stator. The distribution of total pressure losses for the three contributors discussed earlier is given in Table 4 below. Formulation of loss in performance was carried out for all seven stages of the high pressure compressor and are presented in Table 5. These loss estimates were computed with the use of the stage performance formulated from a 69.9 percent speed line, which will be discussed later.

Table 4. Distribution of total pressure losses in the 13th stage.

	CLEAN	%	ERODED	%
Profile	0.0125	24	0.0212	24
Secondary flows	0.0035	6	0.0027	4
Tip clearance	0.0340	70	0.0667	74
Total	0.050	100	0.091	100

Table 5. Computed performance loss in stages.

STAGE	$\Delta\psi$	$\Delta\eta_{st}$	ξ/ξ_o total
10	0.010	0.018	1.10
11	0.036	0.062	1.47
12	0.047	0.079	1.51
13	0.050	0.084	1.51
14	0.113	0.190	2.13
15	0.120	0.200	2.14
16	0.139	0.232	2.23

SECTION 5

MODELING COMPRESSOR RESPONSE

5.1 FORMULATING AN AVERAGED STAGE PERFORMANCE MAP.

The procedure described in the previous section can be used to determine stage performance deterioration when the actual stage performance characteristics are given. This was not the case for the TF33 and J57 engines which were used in these measurements. Therefore, a method was developed to obtain the stage performance map from the overall compressor map. It is important to incorporate a compression efficiency in the method so that off-design performance can be computed. The only available input parameters are assumed to be the compressor map with corresponding overall adiabatic efficiencies. The method outlined below is based on the relationship between a constant rotational speed line and the stage total pressure coefficient curve. The compressor map provides the relationship among mass flow, total pressure rise, and overall efficiencies along constant rotational speed lines. The inlet total pressure was assumed to be atmospheric pressure and the density was chosen to be that at standard conditions. The exit velocity was calculated knowing the inlet conditions, compressor flow areas, and the efficiency. The total pressure increase can be averaged by the number of stages and a pressure coefficient for inlet and exit stages can be averaged. A suitable averaged stage map can then be used in a stage stack-up procedure. Each stage was assumed to have the same performance map but different operating points. The exit conditions can then be calculated from the continuity equation and the definition of total pressure, equations 20 and 21.

$$\frac{\dot{m}}{A_4} = \rho_4 V_4 \quad (20)$$

$$P_{T_4} = P_4 + 1/2 \rho_4 V_4^2 \quad (21)$$

In order to obtain a third equation and thus allow the calculation of density, velocity, and pressure at the exit, the second law of thermodynamics and the definition of polytropic compression efficiency were used (see Appendix C).

The average flow coefficient is computed from the average of inlet and exit velocity divided by tip rotational speed. The average pressure coefficient is computed from the averaged total pressure rise per stage divided by the reduced density, equation 22.

$$\bar{\psi} = \frac{(P_{T4} - P_{T3})}{1/2 N \rho_r U_t^2} \quad \text{where} \quad \rho_r = \frac{2 \rho_3 \rho_4}{\rho_3 + \rho_4} \quad (22)$$

$$N = \# \text{ of stages}$$

By using the reduced density, the method essentially averages the input mechanical energy per stage. Figure 9 shows the computed averaged stage performance map for a 69.9 percent rotational speed line. This map was used to reconstruct the constant speed line of the compressor map by a stage stacking technique described later. A slight adjustment was needed to reproduce the compressor map line. This was due to the lack of available compressor efficiency data which required that estimates of local values be made. From the previous calculations of changes in stage performance an eroded performance map for several stages is given in Figure 10. If stage performance data were available, they would be preferable to an averaged stage map. Also, the above averaged performance map will only yield accurate results for the constant speed line used.

5.2 GENERATING AN ERODED COMPRESSOR MAP FROM STAGE STACKING.

The compressor map for an eroded compressor can be obtained by reversing the procedure described in Section 5.1 and by using blade erosion data. In other words the deteriorated stages are "stacked" to obtain the eroded compressor map. Figure 11 shows the clean 69.9 percent constant speed line and a corresponding eroded line computed using this stage stacking technique. It is assumed that the operating line of the compressor does not shift due to the relatively unchanged fuel controller, combustor,

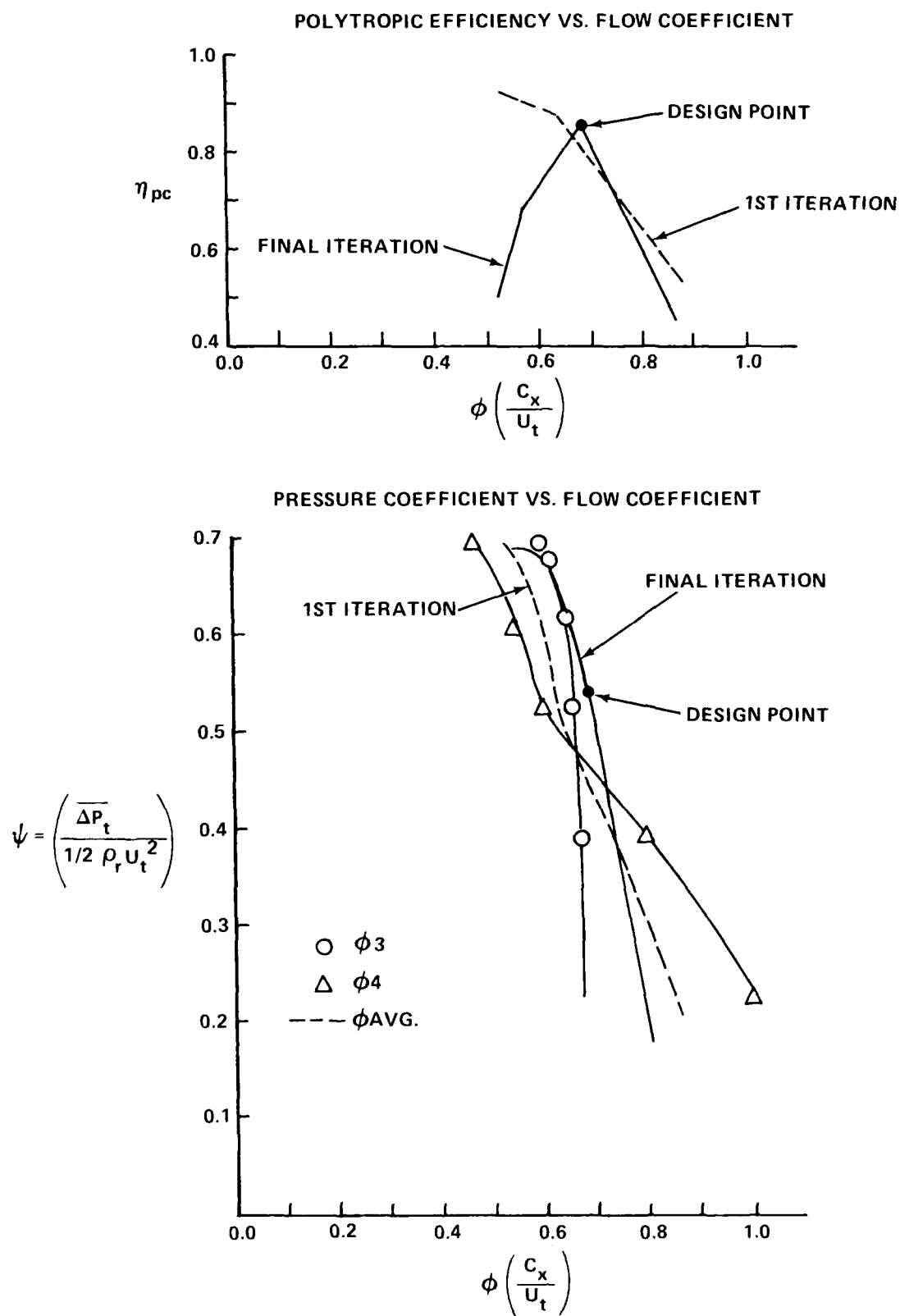


Figure 9. Estimated stage performance map from the 69.9 percent N2 line.

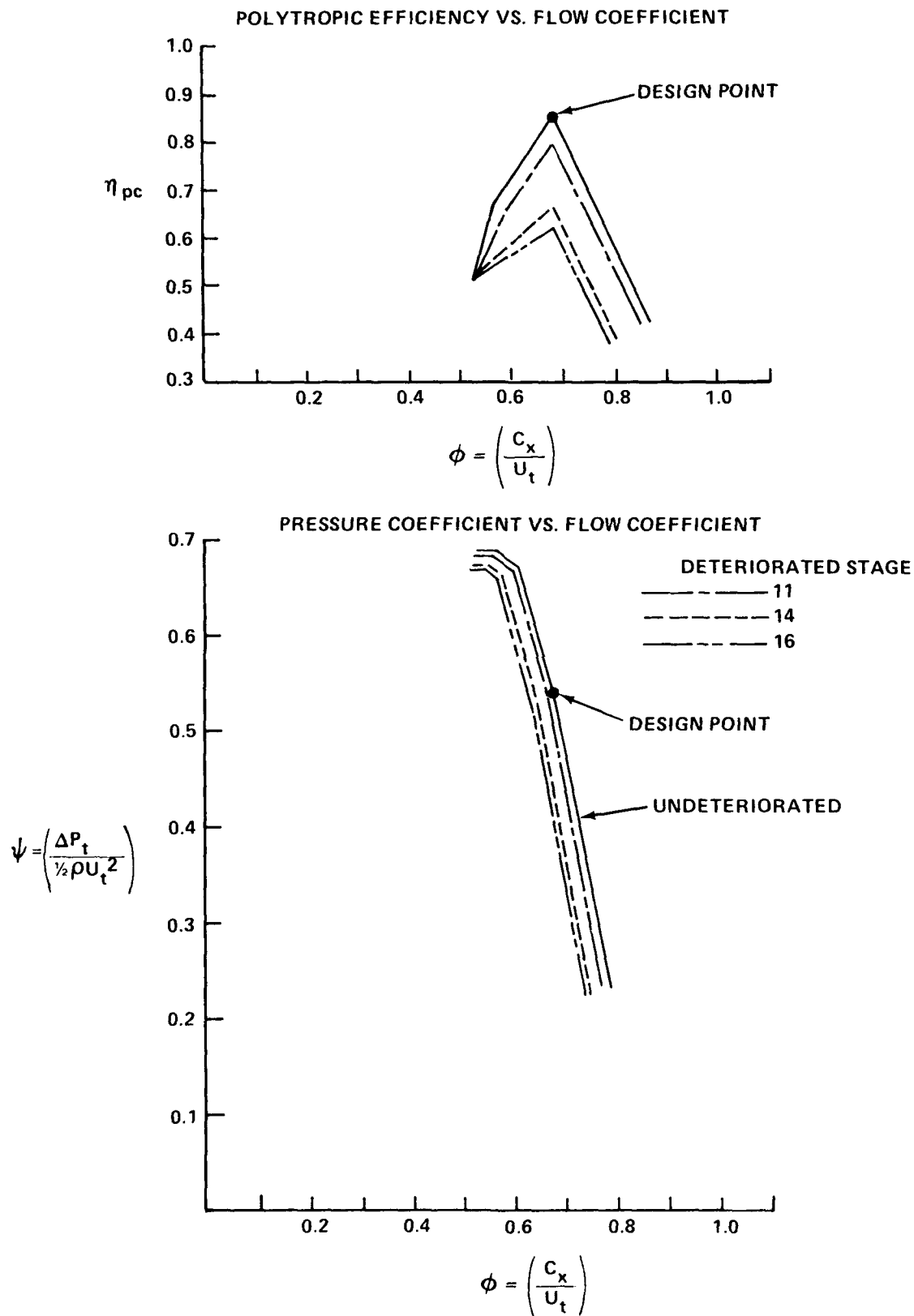


Figure 10. Estimated stage performance deterioration from measured erosions.

and turbine. The shift in speed lines does illustrate a decrease in corrected weight flow and total pressure rise at a constant rotational speed. The loss in corrected weight flow at the constant speed line of 69.9% was computed to be 4.4% of the expected weight flow of the undeteriorated engine at the operating line.

To examine the change in surge line with respect to erosion, a comparison of compressor stability will be made between an undeteriorated and a deteriorated low speed line. For constant properties, the inlet axial velocity is given by the weight flow through the compressor. Therefore, the inlet flow coefficient will be the same for both the deteriorated and undeteriorated speed line at the weight flow corresponding to the undeteriorated compressor surge line. In the case of a low speed surge, the front stages are at high incidence, due to lower flow coefficient, and the back stages are approaching a choking condition. With increasing stage deterioration, the back stages (at the same speed) are experiencing a lower density relative to their uneroded operation. This will cause the exit velocity to be elevated even higher than the uneroded operating value. The deteriorated engine then moves closer to choking the rear stages with the same inlet flow coefficient. With the flow coefficient corresponding to stage stall unchanged for the deteriorated stage, the front stages remain at their unstable high incidence values. It is reasonable to assume then that compressor surge will occur at the same corrected weight flow as that of the undeteriorated compressor at low speed operation. The loss in available surge margin and surge pressure ratio at the 69.9% speed surge point were estimated by equations 23 and 24 and are presented in Table 6 (38). (See Figure 12). The reduction in surge margin is predicted to be 51% while the loss in surge pressure ratio is estimated to be 45%.

$$\Delta SM = \frac{PR_s - PR_o}{PR_o} \quad (23)$$

$$\Delta PRS = \frac{PR_s - PR_o}{PR_s} \quad (24)$$

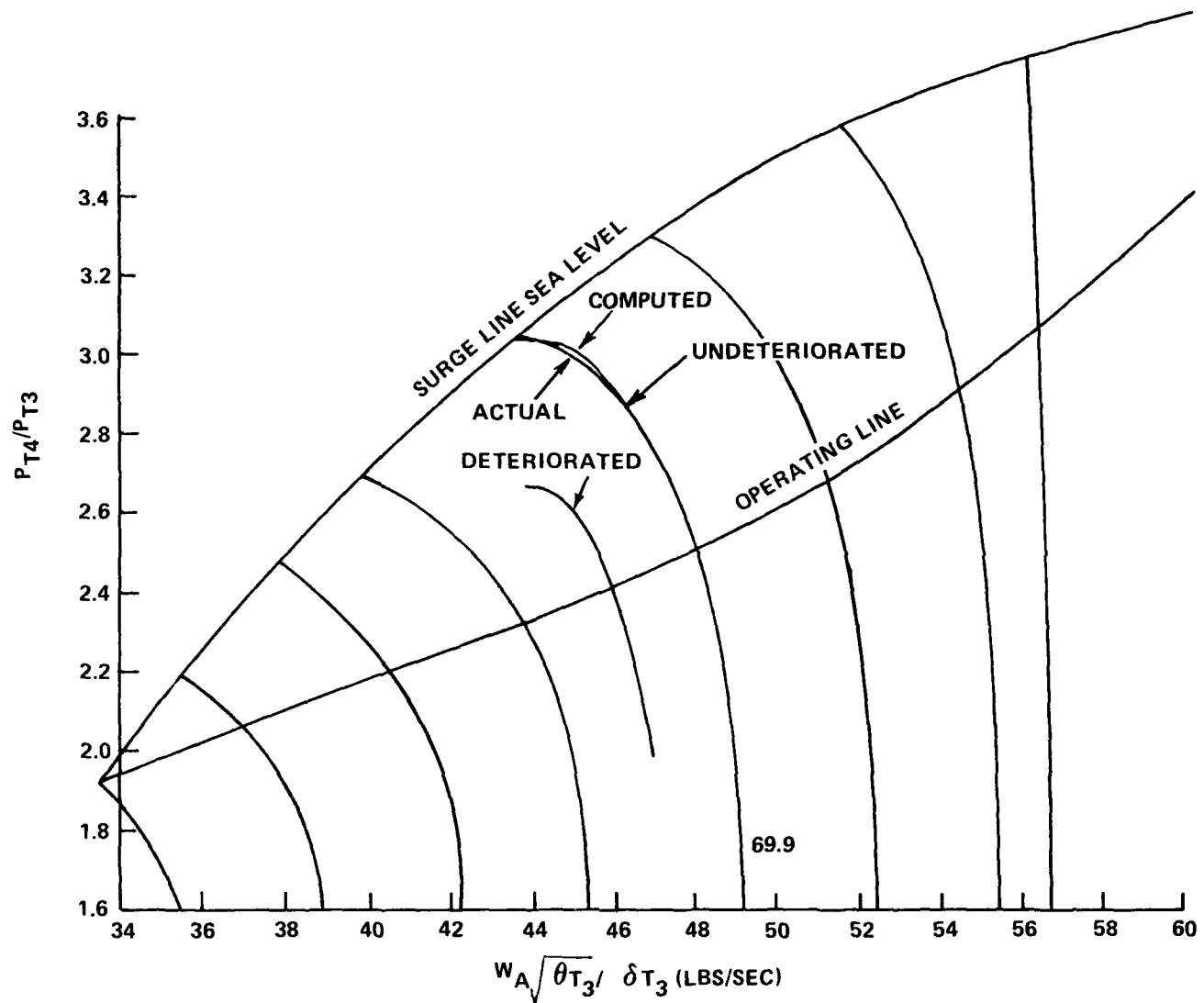


Figure 11. Computed change in compressor performance.

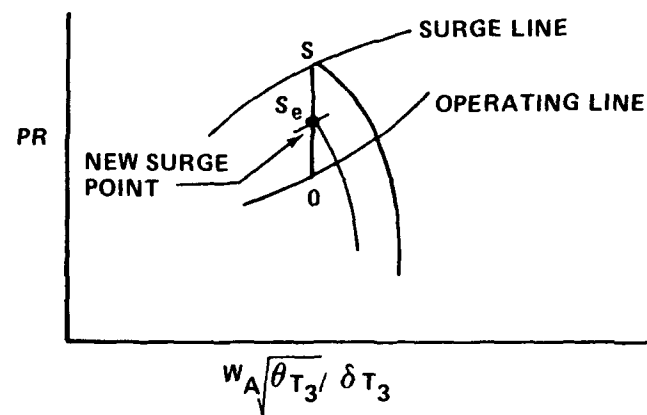


Figure 12. Illustration of surge margin computation.

Table 6. Loss in compressor stability.

	Uneroded	Eroded	% Decrease
ΔSM	.305	.148	51%
ΔPRS	.234	.129	45%

5.3 EFFECT OF LPC AND HPC COUPLING.

In matching the components of a two-spool gas turbine, it is convenient to match the components of the HP spool and then match the HP spool with the LP spool components. In this discussion, the influence of the high pressure compressor (HPC) deterioration on the low pressure compressor (LPC) is described. The matching map for the HP spool, which controls the HP compressor, is altered while sustaining the same operating line. A direct method of matching LP and HP spools is described in (39) and is outlined below in order to illustrate the qualitative aspects of the influence of deterioration on spool matching. Due to the aerodynamic coupling, only two independent conditions are needed to determine the operating points of the components. An operating point is assigned to the HP spool and the LP spool matching is achieved directly. A schematic of the numbering system used is given in Figure 13. The power and continuity relations are expressed with regard to the LPC and LPT, equations 25 and 26.

$$\frac{H_2 - H_1}{N_1^2} - \frac{1}{(1-B_2)(1-B_3)(1+f)} + \frac{P}{W_1(1-B_2)(1-B_3)(1+f)N_1^2} = \frac{H_5 - H_6}{N_1^2} \quad (25)$$

$$\log \frac{W_1 N_1}{\delta_2} = \log \left[\frac{P_5/P_2}{(1-B_2)(1-B_3)(1+f)} \right] + \log \frac{W_5 N_1}{\delta_5} \quad (26)$$

Figures 14 and 15 represent LPC and LPT matching maps, respectively. To match, an inner spool operating point is taken and values of $W_2 \sqrt{\theta_2}/\delta_2$, $W_5 \sqrt{\theta_5}/\delta_5$, and P_5/P_2 are noted on Figure 16. Figures 14 and 15 can be superposed so as to satisfy equations 25 and 26. The ordinates in Figures 14 and 15 are offset by the value of the accessory

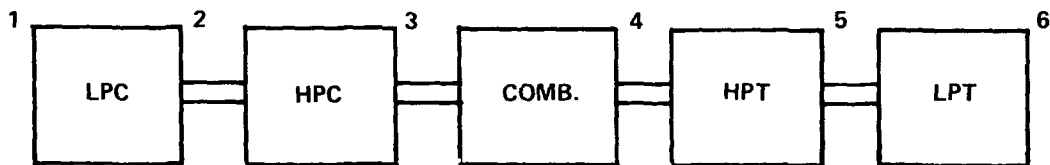


Figure 13. Schematic of numbering system for matching analysis.

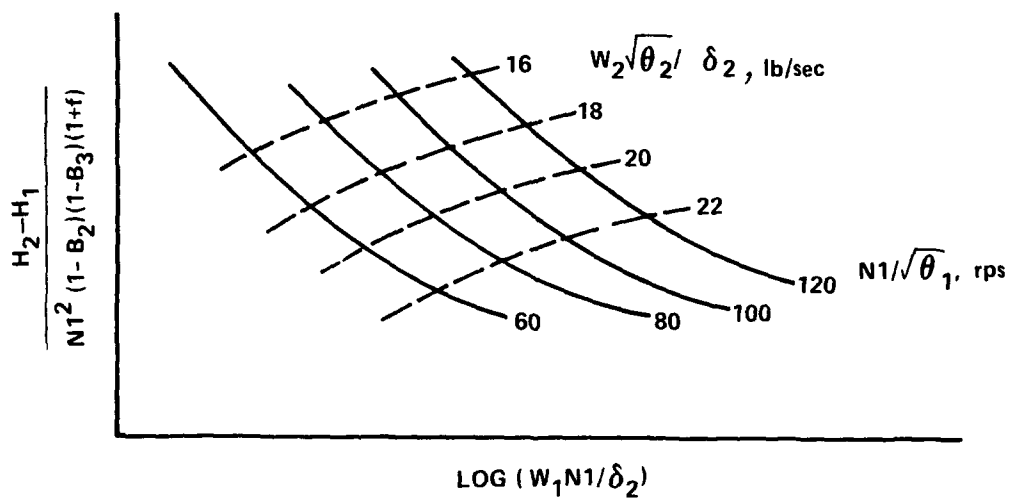


Figure 14. Low pressure compressor matching map.

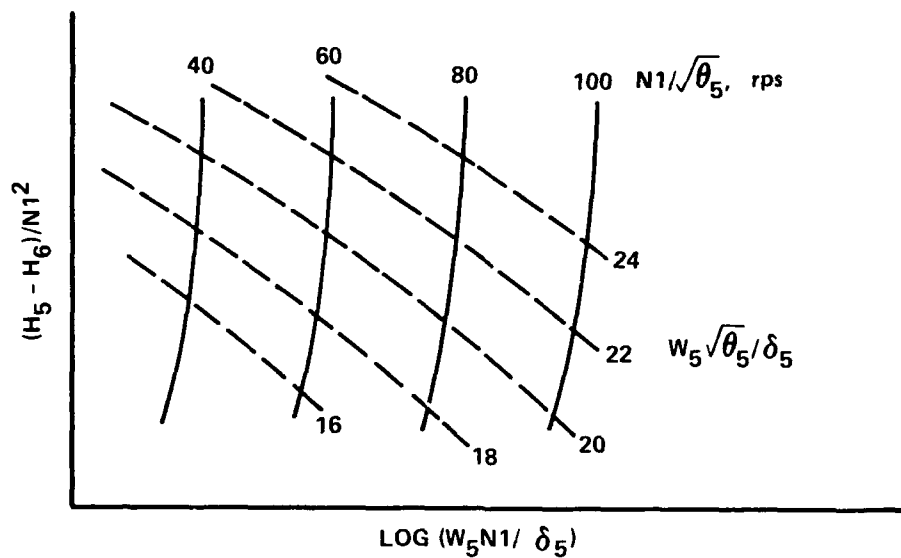


Figure 15. Low pressure turbine matching map.

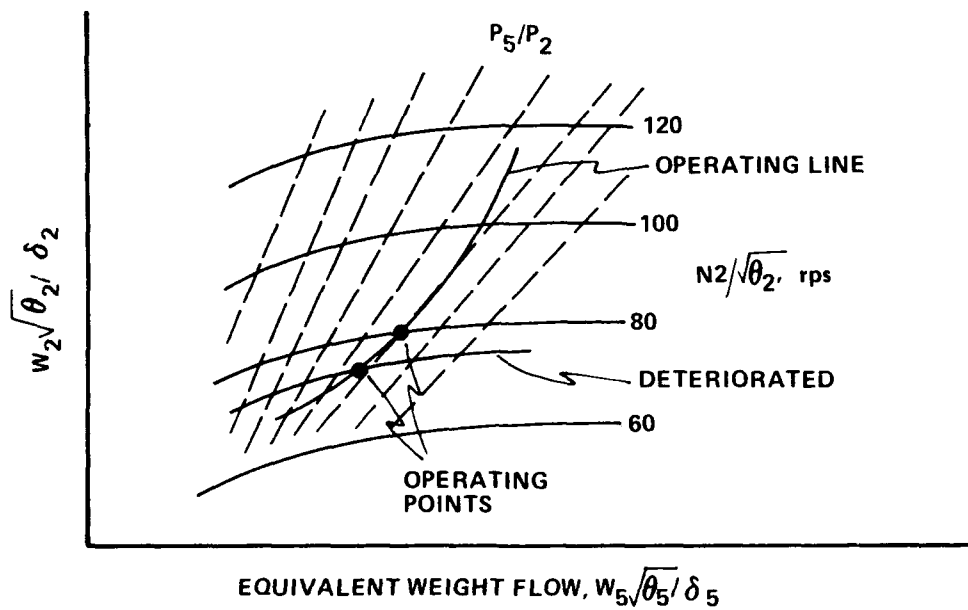


Figure 16. High pressure compressor matching map.

power term in equation 25 and the abscissas are offset by the calculated value of the log $\left[\frac{P_5/P_2}{(1-B_2)(1-B_3)(1+f)} \right]$ term. The operating points of the LPC and LPT corresponding to the selected HP spool operating point are at the intersection of the appropriate lines of constant $W_2\sqrt{\theta_2}/\delta_2$ and $W_5\sqrt{\theta_5}/\delta_5$.

To evaluate the influence of HPC deterioration, the lines of constant N2 are shifted down in Figure 16 and the above procedure is repeated. The LPC and LPT are assumed unchanged so their matching maps are not altered. Note the operating line of Figure 2 is assumed constant so a decrease in $W_2\sqrt{\theta_2}/\delta_2$, $W_5\sqrt{\theta_5}/\delta_5$ and P_5/P_2 is present at a constant inner speed. The accessory power, fuel air ratio, and bypass ratio terms are assumed constant. The decreasing P_5/P_2 value will decrease the difference between the abscissas of Figures 14 and 15. The ordinates are unchanged due to constant accessory power. Figure 17 shows the comparison between the undeteriorated and deteriorated by superposition of Figures 14 and 15. For a constant HP spool speed, the result is a decrease in the LP, spool speed for deteriorated operation. Since the LPT and HPC operating line is assumed unchanged the operating line of the LPC may be assumed constant. This is a valid assumption for either a small shift in the operating line or an operating point which is moving along an unchanged operating line. The change in weight flow through the LPC is given by the continuity relation of equations 27 and 28.

$$\Delta W_1 = \frac{\Delta W_3}{(1-B_2)(1-B_3)} \quad (27)$$

$$\frac{\Delta W_1}{W_1} = \frac{\Delta W_3}{W_3} \quad (28)$$

The deteriorated LP spool speed may be found with the appropriate figures for the given engine.

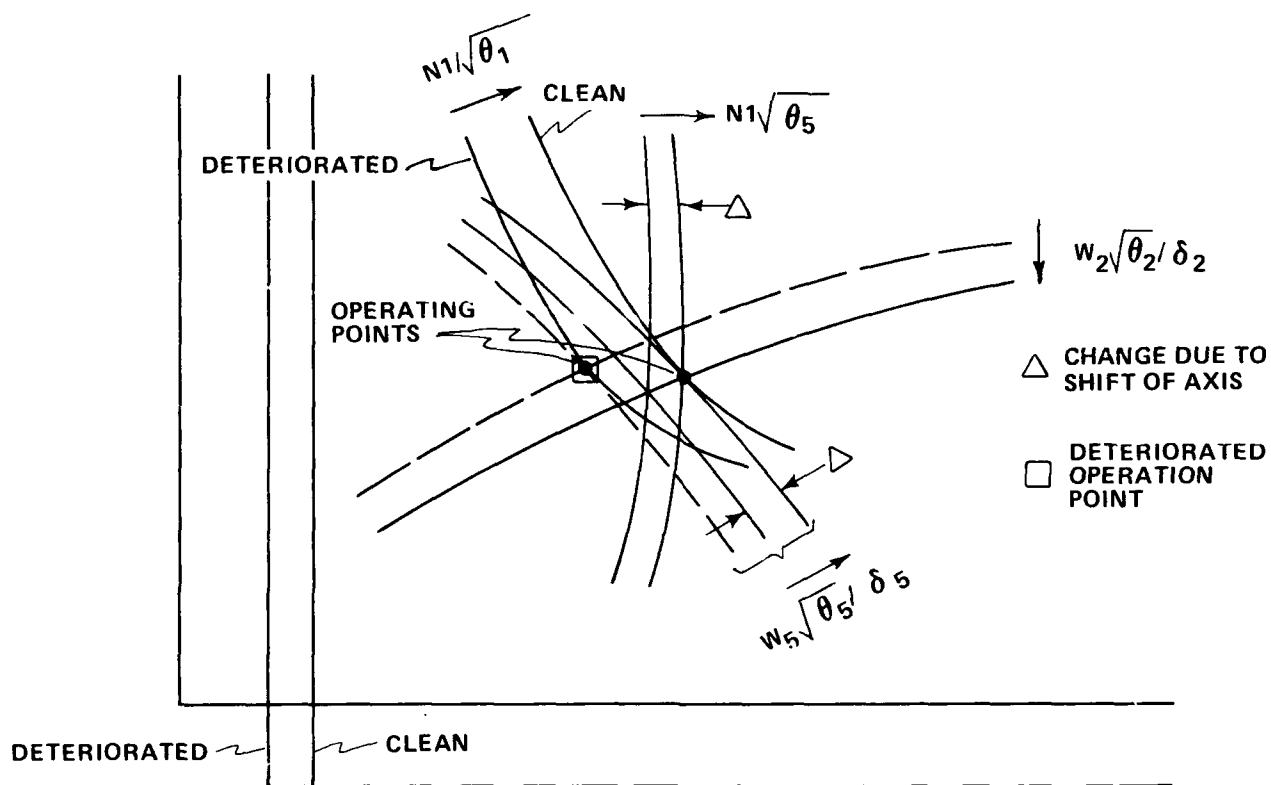


Figure 17. Superposition of LPC and LPT matching maps; deteriorated and undeteriorated.

SECTION 6

DETERIORATED ENGINE RESPONSE

6.1 BLEED AIR CONTROLS.

Given the J57-P19W and TF33-P11A engines, there are two ways the engine operator can alter the compressor inlet and exit conditions to make them less prone to surge. They are the intercompressor bleed and the anti-icing air systems.

The intercompressor bleed is essentially a valve actuated according to a pressure schedule which allows a portion of the air between the two spools to dump overboard. The valve remains open at low speeds, allowing the LPC to essentially freewheel (i.e., accelerate gas but compress it very little). As the engine is accelerated through a scheduled LPC pressure ratio, the valve closes and the spools rematch. Pressure ratio across the LPC rapidly rises and the HPC pressure ratio first falls and then rises with increasing thrust.

By being presented with air at lower density and velocity than if the valve were closed with air at lower density and velocity than if the valve were closed, the HPC is less likely to experience the low-speed front-stage surge generated by high angle of attack from rear stage choking. When the valve does close in normal operation, density and velocity at the high compressor rapidly increase but at this rotor speed the compressor cannot sufficiently compress the air so as to not choke the rear stages. If the HP spool had been turning slower than expected at closing, it would have been more likely to surge.

The anti-ice air system serves to raise the temperature of the metal surface at the face of the engine in order to avoid potentially dangerous ice buildup. The system routes hot air from the cowling downstream of the HPC through a thermally adjusted valve, inside the first fan stator and to the engine inlet. The valve limits the anti-ice flow to only the amount necessary to be effective against the ambient conditions. The amount bled is at most four or five percent of the total flow. By bleeding air from the exit end of the HPC, the anti-ice air system effectively reduces the flow restriction felt by the front stages and moves it away from surge at all speeds; particularly, however, the front stages at low speed.

Both of the systems described above were used during the measurement program to make acceleration to higher power settings possible. They were found to become effective at different deterioration and power levels than each other. One of the TF33s eroded to a point at which it could not be accelerated through a power setting just above idle unless the anti-ice air system was operating. The power setting involved was low enough for the bleed door to be in the open position and any surge in this regime would be in the high pressure compressor front stages. As the compressors eroded, the largest proportionate material loss was in the rear stages. As described in Section 5, severe erosion in the rear stages results in lower densities and higher velocities for a given speed and hence even more of a tendency to choke at low rotational speed.

The amount of air bled for anti-icing is scheduled based on ambient inlet air temperature with larger amounts bled at lower temperatures. This method of surge avoidance, then, may not be effective at high ambient temperatures unless the thermally controlled valve were overridden (which is not a feature of these engines). Anti-ice air did not have a noticeable influence on surge margin other than at the low power settings previously mentioned. Rapid accelerations from midpower to high power levels with anti-ice air both on and off gave essentially identical results.

After further exposure, the TF33 experienced surges at steady state just above the bleed door closing point and a single surge each time it was accelerated through closing. The HPC is operating at nearly its design optimum speed at the time of bleed door closing and is relatively difficult to send into surge. The LPC is at the same time rotating at low speed with relatively little margin and is likely to go to front stage surge.

As erosion progressed, the engine spools rematched to reflect the change in work distribution between them. Typically, the air weight flow for a given engine speed and the low compressor speed for a given EPR decreased. High compressor speed for a given EPR increased. That both low compressor speed and air flow decreased is to be expected in an undamaged compressor and indeed the low spools from the engines were relatively undamaged. The reason the high compressor pumps less at higher speed is examined in Section 5. The role of the fuel controller in the rematch is not clear at this time.

The fuel controller sets fuel flow based on a preset schedule of HPC speed, burner pressure, and power lever angle (PLA). A sketch of a fuel controller map is shown in Figure 18. For a given PLA, the controller maintains a fixed fuel flow-to-burner pressure ratio and a fixed compressor speed by metering fuel to the combustor. Whenever the power setting is above cruise, burner pressure is constant and the controller adjusts fuel flow to maintain control speed. For power settings below cruise, fuel flow, burner pressure, and speed all increase with increasing power. Fuel flow increases faster than burner pressure with increasing speed.

It is felt the fuel controller contributed to the quasi-steady state surge described in Section 2.7. During the hour preceding surge, the PLA was increased several times to compensate for decreasing EPR. HPC speed had remained constant and both fuel flow and burner pressure had been falling. Each time the PLA was adjusted, burner pressure increased to its "pre-fall" value and fuel flow exceeded its value. On the fuel control map this is represented by a leftward shift of the constant PLA lines and a new operating point above the operating line. The fuel controller response can be either to cut fuel flow (which it did several times initially) or to search for a new one line operating point at a higher speed (which it did before going into surge). This would mean the instantaneous operating point would move to the left and the fuel flow would begin to increase to return to the line. If this increased burner pressure sufficiently to overpower the exit pressure of the HPC, then surge would occur.

6.2 DETERIORATION IN WEIGHT FLOW.

The experimental data taken during testing of the third TF33 will be evaluated for comparison with clean air baseline data. The baseline weight flow versus rotational speed plot was generated from the first three clean air calibration (run nos. 94, 95, 96). A fourth order polynomial fit, Figure 19, was performed on the baseline data with a 99% confidence interval of $\Delta |W_a \sqrt{\theta_{T2}} / \delta_2| = 4.38 \text{ lbs/sec}$. The deviation from the baseline curve was then evaluated as dust ingestion progresses. It is expected that as ingestion of dust progresses the weight flow of air through the engine will decrease with respect to rotational speed. The deviation of experimental data from the baseline curve is normalized by the Z statistic corresponding to a 99% confidence interval for an assumed standard normal distribution. Figure 20 illustrates the normalized distribution of weight flow in order of increasing cumulative dust ingested. A significant

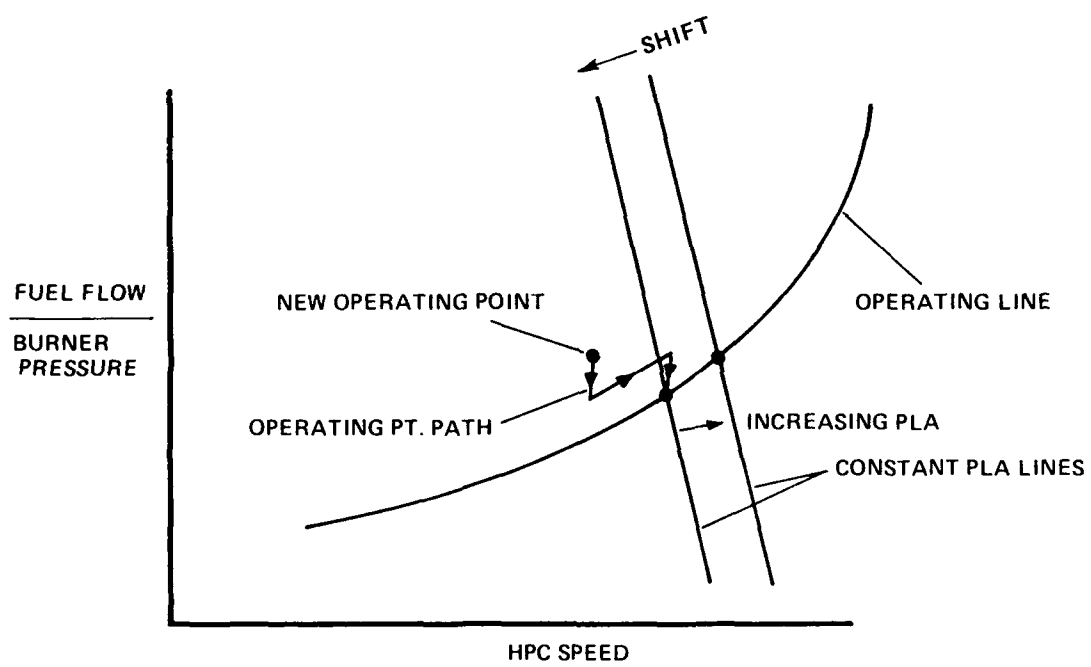


Figure 18. Fuel controller map.

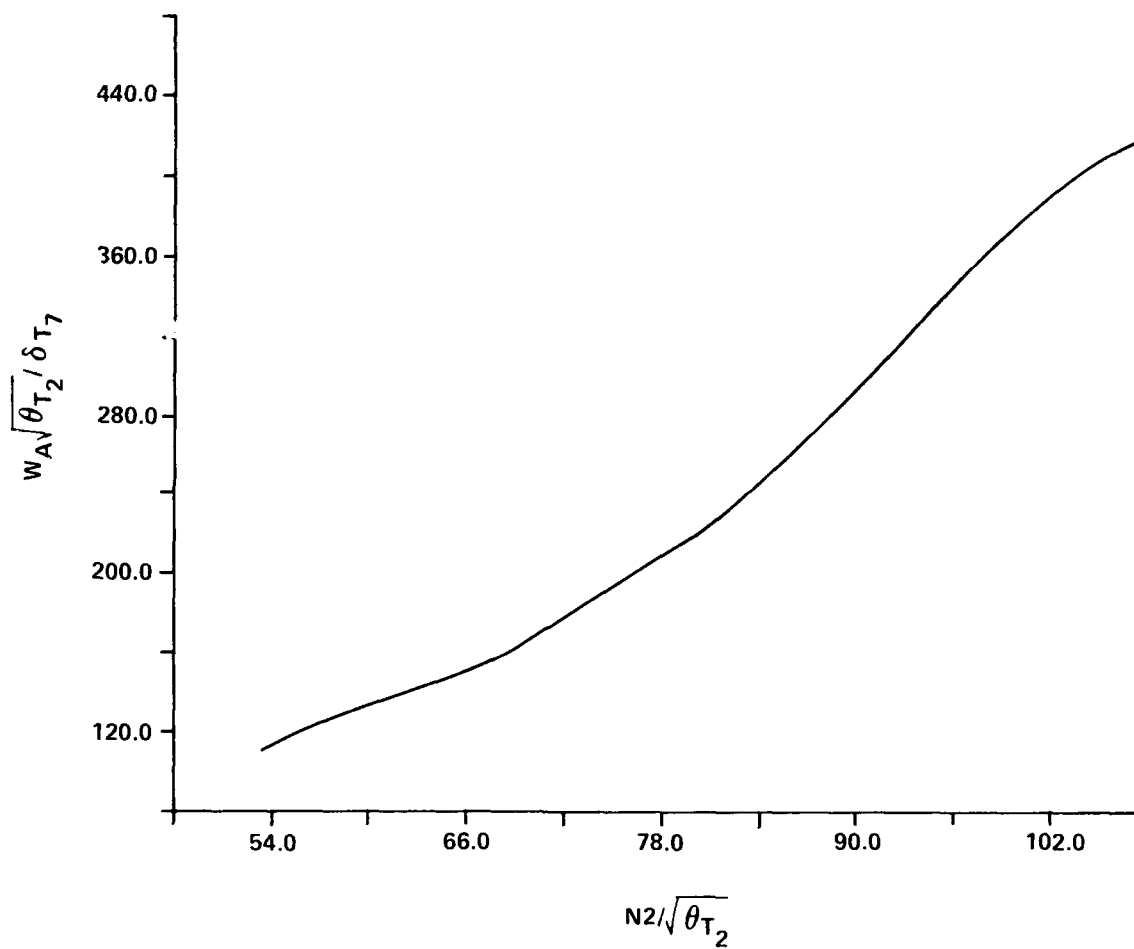


Figure 19. Fourth order polynomial fit to the pre-exposure calibration data.

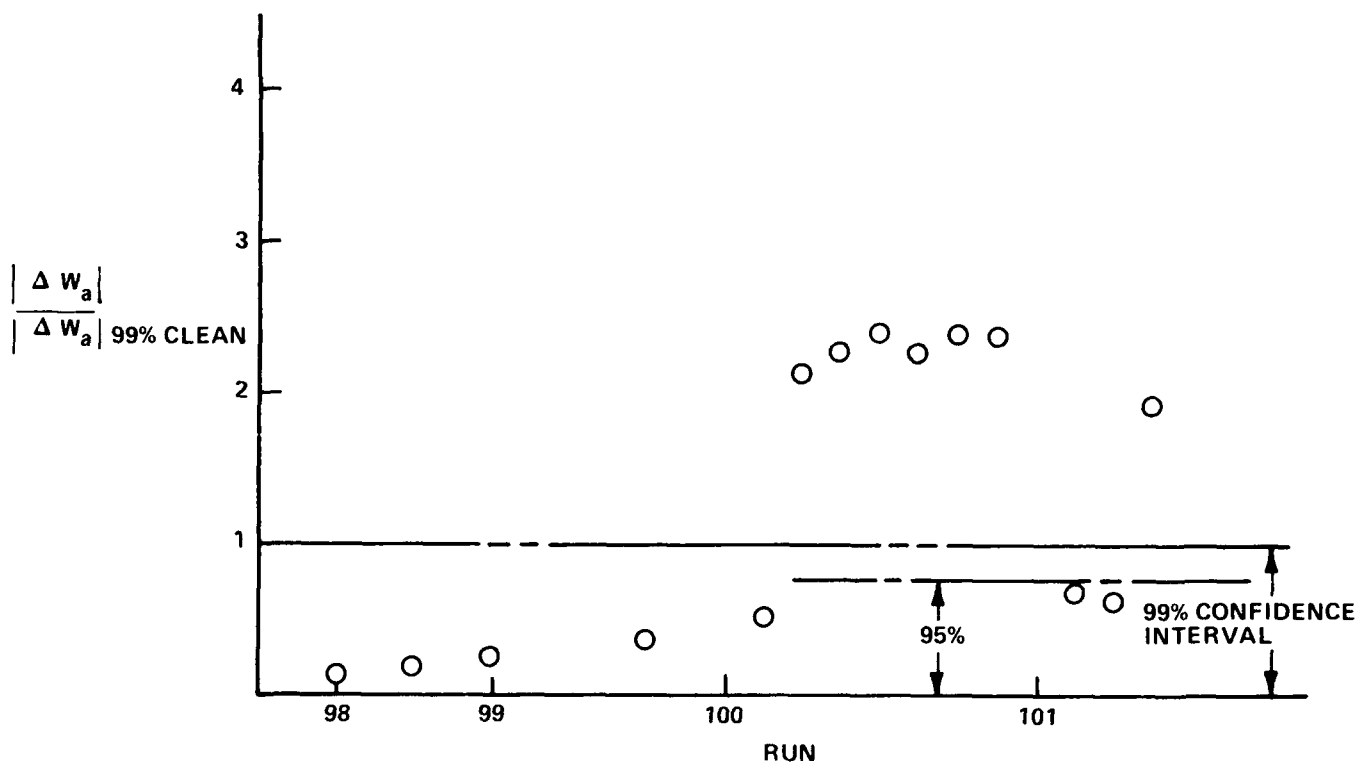


Figure 20. Deviation from baseline weight flow vs. rotational speed curve.

number of data points fall outside the undeteriorated 99% confidence interval indicating a change in engine performance outside the computed fluctuations of the undeteriorated data.

The predicted decrease in corrected weight flow at $N_2/\sqrt{\theta_T}$ of 69.9% speed is at a normalized deviation of 1.71. This value represents the average expected for a sample of data at 69.9% rotational speed. By assuming that the standard deviation of the data for the deteriorated engine is equal to the standard deviation of the undeteriorated engine, we may compute the 99% confidence interval of the deteriorated performance. Note that the predicted value corresponds to the last run since the measured erosions were taken from the blades of a torn down engine. Figure 21 shows the predicted deteriorated 99% confidence interval and associated sampled data points for the last few runs. The majority of the sampled data does fall within the 99% confidence interval predicted and indicates good agreement with predicted results. Some of the dispersion of the data may be due to the fact that the majority of the data were sampled at the design speed and the calculations were performed for the 69.9% speed value. It is not possible to determine the functional dependence of deviation from the baseline curve on rotational speed due to the limited range of power settings sampled.

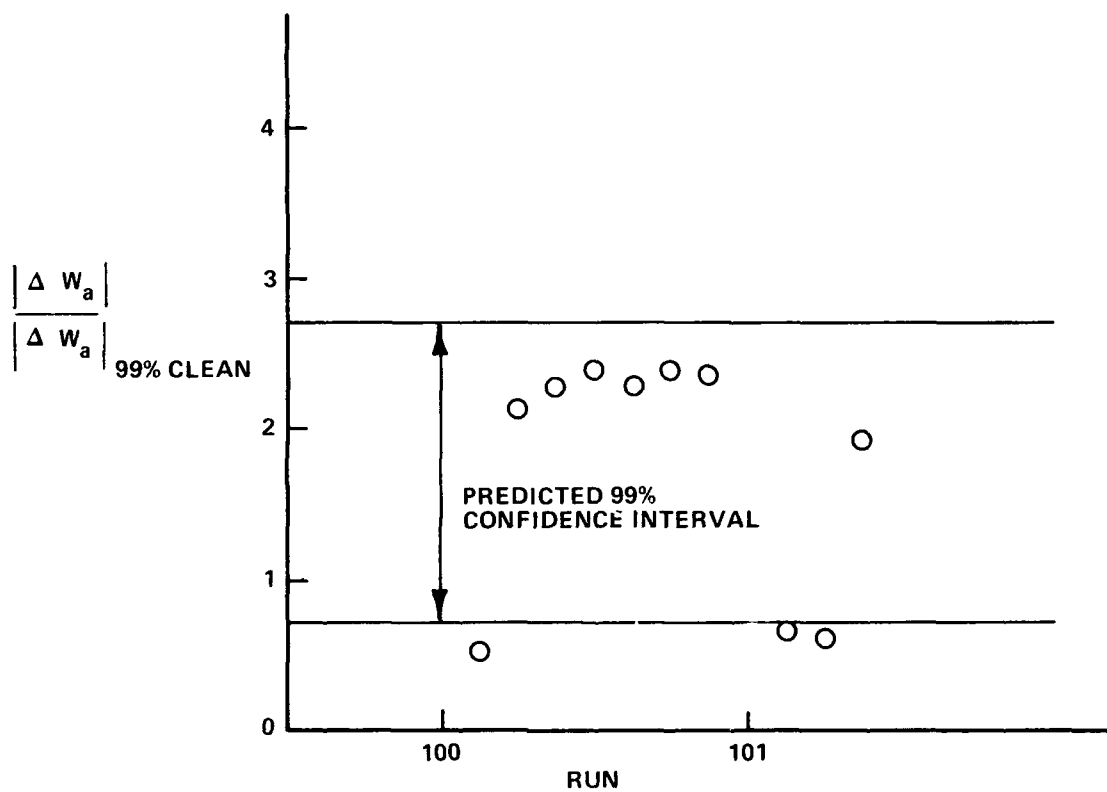


Figure 21. Comparison of predicted deterioration with experimental data.

SECTION 7

CONCLUSION

A measurements program currently underway at Arvin/Calspan has been used in the evaluation of observed engine behavior during dust ingestion. The major effect of solid particle ingestion was the erosion and subsequent performance deterioration of the HPC. The most noticeable feature of blade removal was increased tip clearance and blade leading edge erosion. The increase in proportionate blade loss through the compressor will result in substantial performance deterioration in both the LPC and HPC stages.

The observations obtained from the analysis and data described in this report indicate that a deteriorated engine will be increasingly likely to surge when low speed acceleration is initiated. Indications of deterioration were found to be reduced burner pressure and air weight flow for a given HPC speed. In an eroded engine before the final stage of deterioration, the intercompressor bleed and anti-ice air served to decrease the susceptibility to surge at low power settings. Specifically, use of anti-ice air can serve to decrease the likelihood of off-idle surges; use of intercompressor override can serve to avoid surge at bleed door closing. Off-idle surges emanate from the HPC and intercompressor bleed door closing surge emanates from the LPC. The influence of erosion is to make the front stages of the HPC and LPC more prone to surge. It was also observed that near cruise power the fuel controller can send a deteriorated engine, while operating at steady state and having a narrow surge margin, into a autoacceleration and surge.

To quantify the performance deterioration a predictive capability was developed based on a semiempirical method. The individual stages were modeled to evaluate the effects of increased tip clearance and leading edge effects. The change in total pressure rise and efficiency for the undivided stages were calculated and used to develop new performance maps. The stages were then stacked to arrive at a deteriorated compressor map. The qualitative effect of shifting the constant speed lines toward reduced mass flow and lower pressure ratio is in agreement with experimental observations. The quantitative results of reduction in corrected weight flow gave good agreement with experimental data. The reduction in surge margin at the 69.9% N2 surge line was predicted to be 51%. Although quantitative measurements

of surge margin are not available, the observed engine behavior does agree with the expected results of such a loss.

SECTION 8

LIST OF REFERENCES

1. Mitchell, H.J. and Gilmore, F.R., "Dust-Cloud Effects on Aircraft Engines - Emerging Issues and New Damage Mechanisms," RDA-TR-120012-001, March 1982.
2. Chambers, J.C., "The 1982 Encounter of British Airways 747 with the Mt. Galunggung Eruption Cloud," AIAA Paper 85-0097, AIAA 23rd Aerospace Sciences Meeting, 14-17 January 1985, Reno, Nevada.
3. Tabakoff, W. and Hussein, M.F., "Effects of Suspended Solid Particles on the Properties in Cascade Flow," AIAA Journal, August 1971, pp. 1514-1519.
4. Tabakoff, W. and Hussein, M.F., "Pressure Distribution on Blades in Cascade Nozzle for Particulate Flow," Journal of Aircraft, September 1971, pp. 736-738.
5. Hussein, M.F. and Tabakoff, W., "Dynamic Behavior of Solid Particles Suspended by Polluted Flow in a Turbine Stage," Journal of Aircraft, July 1973, pp. 434-440.
6. Grant, G., and Tabakoff, W., "Erosion Prediction of Turbomachinery Resulting from Environmental Solid Particles," Journal of Aircraft, May 1975, pp. 471-478.
7. Tabakoff, W. and Bahan, C., "Effects of Solid Particles Suspended in Fluid Flow Through an Axial Flow Compressor Stage," Paper presented at the 5th International Symposium on Airbreathing Engines, February 16-21, 1981, Bangalore, India.
8. Tabakoff, W., "Compressor Erosion and Performance Deterioration," AIAA/ASME 4th Joint Fluid Mechanics, Plasma Dynamics, and Lasers Conference, Atlanta, Georgia, May 12-14, 1986.
9. Hamed, A., "Effect of Particle Characteristics on Trajectories and Blade Impact Patterns," AIAA/ASME 4th. Joint Fluid Mechanics, Plasma Dynamics, and Laser Conference, Atlanta, Georgia, May 12-14, 1986.
10. Dunn, M.G., Padova, C., and Moller, J.C., "Performance Deterioration of an Operational TF33 Turbofan Engine Upon Exposure to a Simulated Nuclear Dust Environment," DNA-TR-86-62-V1, January 1986.
11. Dunn, M.G., Padova, C., and Moller, J.C., "Performance Deterioration of Turbojet Engine Upon Exposure to a Dust Environment," DNA TR-86-62-V2, July 1986.
12. Dunn, M.G., Padova, C., and Moller, J.C., "Deterioration of a TF33 Turbofan When Exposed to a Scoria-Laden Dust Environment," DNA-86-62-V3, August 1986.

13. Finnie, I., "The Mechanism of Erosion of Ductile Metals," ASME Proceedings of Applied Mechanics, pp. 527-532, 1958.
14. Finnie, I., Wolak, J., and Kabil, Y., "Erosion of Metals by Solid Particles," Journal of Materials, Vol. 2, pp. 692-700, 1967.
15. Goodwin, J.E., Sage, W., and Tilly, G.P., "Study of Erosion by Solid Particles," Proceedings of the Institute of Mechanical Engineers, Vol. 184, Pt. 1, pp. 279-292, 1969-70.
16. Tilly, G.P. and Sage, W., "The Interaction of Particle and Material Behavior in Erosion Processes," Wear, Vol. 16, pp. 447-465, 1970.
17. Rao, P.V. and Buckley, D.H. "Characterization of Solid Particle Erosion Resistance of Ductile Metals Based on Their Properties," Journal of Engineering for Gas Turbines and Power, Vol. 107, pp. 669-678, 1985.
18. Rao, P.V. and Buckley, D.H. "Effect of Surface Configuration During Solid Particle Impingement Erosion," Journal of Engineering for Gas Turbines and Power, Vol. 107, pp. 661-667, 1985.
19. Sheldon, G.L. and Kanhere, A., "An Investigation of Impingement Erosion Using Single Particles," Wear, Vol. 21, pp. 195-209, 1972.
20. Sheldon, G.L., and Finnie, I., "On the Ductile Behavior of Nominally Brittle Materials During Erosive Cutting," Journal of Engineering Industry, pp. 387-392, Nov. 1966.
21. Sargent, G.A., Mehrotra, P.K., and Conrad, H., "Multiparticle Erosion of Pyrex Glass," Erosion: Prevention and Useful Applications, ASTM STP 664 (W.F. Adler, ed.) American Society for Testing Materials, 77-100, 1979.
22. Tabakoff, W., Malak, M.F., and Hamed, A., "Laser Measurements of Solid Particles Rebound Parameters Impacting on 2024 Aluminum and 6Al-4V Titanium Alloys," AIAA-85-1570 Paper presented at the 18th Fluid Dynamics Conference, Cincinnati, Ohio, July 1985.
23. Tabor, D., "The Hardness of Metals", 1st ed., Clarendon Press, Oxford, England, 1951.
24. Head, W.J., "The Development of a Model to Predict the Erosion of Materials by Natural Contaminants," Ph.D. thesis, Dept. of Civil Engineering, Purdue University, West Lafayette, IN., 1970.
25. Hamed, A., Tabakoff, W., and Mansour, M.L., "Turbine Erosion Exposed to Particulate Flow," ASME Paper 86-GT-258 presented at the International Gas Turbine Conference and Exhibit, Dusseldorf, West Germany, June 8-12, 1986.

26. Inove M., Kuroumaru M., Fukuhara M.; "Behavior of Tip Leakage Flow Behind an Axial Compressor Rotor"; ASME Journal of Gas Turbines and Power, Jan 1986, No. 85-GT62, Vol 108, pp 7-37.
27. Senoo, Y., Ishida, M.; "Pressure Loss Due to the Tip Clearance of Impeller Blades in Centrifugal and Axial Blowers", ASME Journal for Gas Turbines and Power, Jan 1985, No. 85-GT-196, Vol 108, pp 32-37.
28. Lakshminarayana B., Sitaram N., Zhang J.; "End-Wall and Profile Losses in a Low-Speed Axial Flow Compressor Rotor"; ASME Journal of Gas Turbines and Power, Jan 1986, No. 85-GT174, Vol 108, pp 22-31.
29. Lakshminarayana, B., "Methods of Predicting the Tip Clearance Effects in Axial Flow Turbomachinery," ASME Journal of Basic Engineering, Vol. 92, No. 9, 1970, pp 467-482.
30. Hah C., "A Numerical Modeling of Endwall and Tip-Clearance Flow of an Isolated Compressor Rotor", ASME Journal of Engineering for Gas Turbines and Power, No. 85-GT-116, Jan 86, Vol. 108, pp 15-21.
31. Khabba G., Senoo Y., "The Influence of Tip Clearance on Stall Limits of a Rectilinear Cascade of Compressor Blades", ASME Journal of Basic Engineering, Sept. 1961, pp 371-378.
32. McNair, R.E., "Tip Clearance Effects on Stalling Pressure Rise in Axial Flow Compressors", ASME Symposium on Compressor Stall, Surge, and System Response, March 1960, pp 47-50.
33. Anderson, J.D., Fundamentals of Aerodynamics, McGraw-Hill, 1984, pp 212-217.
34. Horlock, J.H., Axial Flow Compressors, Fluid Mechanics and Thermodynamics; Krieger, 1973, pp 29-45.
35. Hawthorne, W.R., Aerodynamics of Turbines and Compressors, Princeton University Press, 1964, Section B.
36. Hill, P. and Peterson, C., Mechanics and Thermodynamics of Propulsion, Addison-Wesley Publishing Company, 1965, pp 238-312.
37. Howell A.R., NACA Members of Compressor and Turbine Research Division Aerodynamic Design of Axial-Flow Compressors. NACA RME 56B03b (1956). (Revised) NASA S.R. 36 (1965).
38. Oates, G.C., The Aerothermodynamics of Aircraft Gas Turbine Engines, AF APL-TR-78-52, cpt 23.
39. Dugan, J.F., "Compressor and Turbine Matching," in Aerodynamic Design of Axial-Flow Compressors, National Aeronautics and Space Administration, NASA SP-36, 1965, Chapt. XVII.

APPENDIX A DEVELOPMENT OF ERODED LIFT COEFFICIENT

For contributions due to camber, the classical thin airfoil assumptions yield equation A-1;

$$C_{l_c} = 2 \int_0^\pi \frac{dz_o}{dx} (\cos \theta - 1) d\theta \quad (A-1)$$

where

$$\frac{x}{c} = 1/2 (1 - \cos \theta)$$

$$\frac{dz}{dx} = \text{slope of mean camber line}$$

By examining the airfoil section as it erodes at the leading edge, an eroded camber line may be formulated in terms of the clean camber line and a change in chord (see Figure 22).

$$\frac{z'}{c} = \cos (\Delta\alpha) \left[\left[\frac{z_o}{c} \right]_x - E(\Delta c) \left(1 - \frac{x}{c} \right) \right] \quad (A-2)$$

$$\cos (\Delta\alpha) = \frac{(1 - \frac{\Delta c}{c})}{\left[(1 - \frac{\Delta c}{c})^2 + \left[\frac{z_o}{c} \right]_{\Delta c} \right]^{1/2}} \quad (A-3)$$

$$\Delta\alpha = \arctan \left\{ E(\Delta c) \right\} \quad (A-4)$$

where

$$E(\Delta c) = \frac{\left[\frac{z_o}{c} \right]_{\Delta c}}{1 - \frac{\Delta c}{c}}$$

Since the inlet fluid angle is not changed, the effect of the increased angle of the chord line is felt in the camber angle used in the derivation of thin airfoil theory (see Figure 23). The camber line used is defined by a chord line in the horizontal plane. As the chord changes the camber decreases and the integration is taken from θ_ϵ to π , where $\theta_\epsilon = \arccos(1 - 2 \Delta c/c)$. Equation A-5 formulates the contribution to lift coefficient from the eroded camber line.

$$C_{l_c}' = 2 \int_{\theta_\epsilon}^{\pi} \frac{dz'}{dx} (\cos \theta - 1) d\theta \quad (A-5)$$

To compute the change in blade lift coefficient, equation A-5 is subtracted from equation A-1 which will eliminate biasing felt by the classical thin airfoil theory assumptions resulting in equation A-6.

$$\Delta C_l = 2 \int_0^{\theta_\epsilon} \frac{dz}{dx} (\cos \theta - 1) d\theta + 2 \int_{\theta_\epsilon}^{\pi} \left[\frac{dz_o}{dx} - \frac{dz'}{dx} \right] (\cos \theta - 1) d\theta \quad (A-6)$$

where

$$\frac{dz_o}{dx} - \frac{dz'}{dx} = -E(\Delta c) \cos \Delta \alpha \left(\frac{x}{c} \right) - \frac{dz_o}{dx} (\cos \Delta \alpha - 1) \quad (A-7)$$

Only small changes in chord are of interest here and thus the above equations can be simplified.

where

$$\begin{aligned} \frac{\Delta c}{c} &< 1 \\ \cos(\Delta \alpha) &\approx 1 \\ \theta_\epsilon &\approx 0 \\ \Delta C_l &= 2 \int_0^{\pi} -E(\Delta c) \left(\frac{x}{c} \right) (\cos \theta - 1) d\theta \end{aligned} \quad (A-8)$$

Equation A-8 can be integrated noting that $E(\Delta C)$ is a constant for any given eroded state to obtain equation A-9.

$$\Delta C_{\ell} = 1.5 \pi E(\Delta c) \quad (A-9)$$

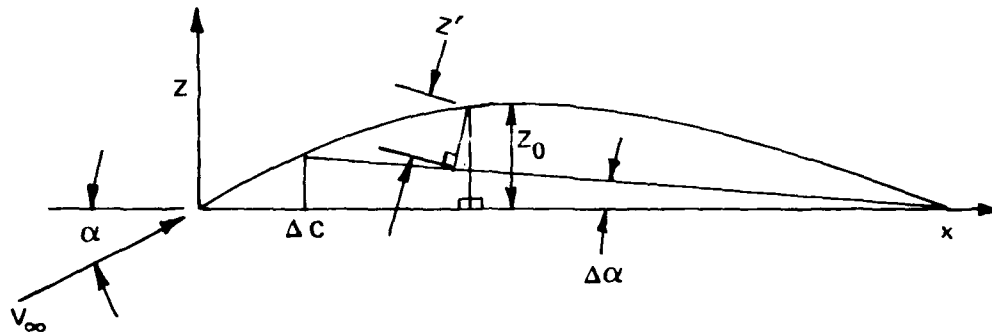


Figure 22. Formulating changes of the mean camber line.

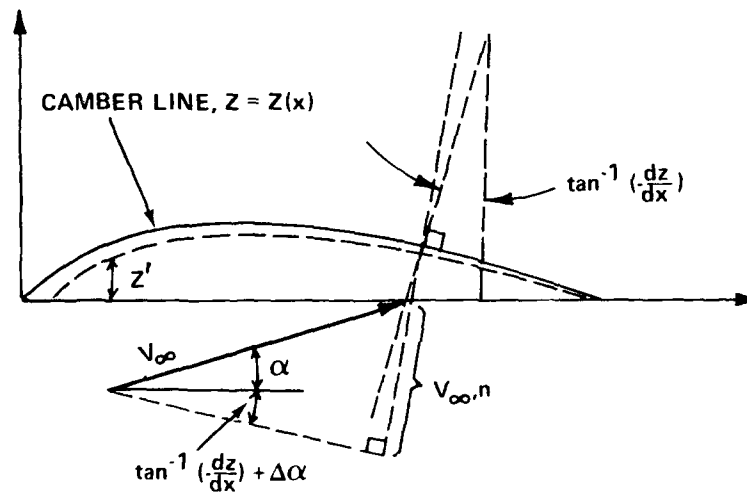


Figure 23. Modified thin airfoil theory.

APPENDIX B AN APPROXIMATE POTENTIAL FLOW SOLUTION FOR A THIN HIGHLY CAMBERED AIRFOIL

The method described below is an extension to classical thin airfoil theory without the assumptions of small angle of attack and small camber angle. For purposes of evaluation of the perturbation velocity (u, w) the sheet vortex is taken to lie on the x -axis, in the range $0 \leq x \leq c$, rather than on the line $z = z(x)$. This is the only assumption of the solution and makes use of the fact that $|z(x)| \ll c$.

The boundary condition at the surface of the camber line is a zero normal velocity

$$v_{\infty, n} + W' (S) = 0 \quad (B-1)$$

From Figure 25 equation B-2 is formulated

$$v_{\infty, n} = v_{\infty} \sin \left[\alpha + \tan^{-1} \left(- \frac{dz}{dx} \right) \right] W' (S) \quad (B-2)$$

$$W(x) = \cos \left[\tan^{-1} \left(\frac{dz}{dx} \right) \right] W' (S) \quad (B-3)$$

From the derivation of $W(X)$ (33) we have equation B-4.

$$\frac{1}{2\pi} \int_0^c \frac{\gamma(\xi) s \xi}{x - \xi} = v_{\infty} \sin \left[\alpha + \tan^{-1} \left(- \frac{dz}{dx} \right) \right] \cos \left[\tan^{-1} \left(\frac{dz}{dx} \right) \right] \quad (B-4)$$

Transform via

$$\xi = \frac{c}{2} (1 - \cos \theta)$$

$$d\xi = \frac{c}{2} \sin \theta d\theta$$

$$x = \frac{c}{2} (1 - \cos \theta_0)$$

$$\frac{1}{2\pi} \int_0^\pi \frac{\gamma(\theta) \sin \theta d\theta}{\cos \theta - \cos \theta_0} = v_\infty \sin \left[\alpha + \tan^{-1} \left(-\frac{dz}{dx} \right) \right] \quad (B-5)$$

$$\times \cos \left[\tan^{-1} \left(\frac{dz}{dx} \right) \right]$$

A solution for $\gamma(\theta)$ is obtained subject to the Kutta condition $\gamma(\pi) = 0$. This solution will make the camber line a streamline of the flow. The solution is presented below (33).

$$\frac{1}{\pi} \int_0^\pi \frac{A_0 (1 + \cos \theta) d\theta}{\cos \theta - \cos \theta_0} + \frac{1}{\pi} \sum_{n=1}^{\infty} \int_0^\pi \frac{A_n \sin n\theta \sin \theta d\theta}{\cos \theta - \cos \theta_0}$$

$$= \sin \left[\alpha + \tan^{-1} \left(-\frac{dz}{dx} \right) \right] \cos \left[\tan^{-1} \left(\frac{dz}{dx} \right) \right]$$

Using:

$$\int_0^\pi \frac{\cos n\theta d\theta}{\cos \theta - \cos \theta_0} = \frac{\pi \sin n\theta_0}{\sin \theta_0}$$

$$\int_0^\pi \frac{\sin n\theta \sin \theta d\theta}{\cos \theta - \cos \theta_0} = -\pi \cos n\theta_0$$

The following is obtained

$$A_0 - \sum_{n=1}^{\infty} A_n \cos n\theta_0 = \sin \left[\alpha + \tan^{-1} \left(-\frac{dz}{dx} \right) \right] \cos \left[\tan^{-1} \left(\frac{dz}{dx} \right) \right]$$

Note the similarity to the Fourier cosine series given below.

$$f(\theta) = B_0 + \sum_{n=1}^{\infty} B_n \cos n\theta$$

$$B_0 = \frac{1}{\pi} \int_0^\pi f(\theta) d\theta$$

$$B_n = \frac{2}{\pi} \int_0^\pi f(\theta) \cos n\theta d\theta$$

where $f(\theta)$ is analogous to

$$\sin \left[\alpha + \tan^{-1} \left(- \frac{dz}{dx} \right) \right] \cos \left[\tan^{-1} \left(\frac{dz}{dx} \right) \right]$$

where

$$A_0 = \frac{1}{\pi} \int_0^\pi \sin \left[\alpha + \tan^{-1} \left(- \frac{dz}{dx} \right) \right] \cos \left[\tan^{-1} \left(\frac{dz}{dx} \right) \right] d \theta_0$$

$$A_n = \frac{-2}{\pi} \int_0^\pi \sin \left[\alpha + \tan^{-1} \left(- \frac{dz}{dx} \right) \right] \cos n \theta_0 d \theta_0$$

It may also be shown that the lift coefficient of the airfoil is given by equation B-6 (33).

$$C_L = \pi (2 A_0 + A_1) \quad (B-6)$$

Let

$$F(x) = \sin \left[\alpha + \tan^{-1} \left(- \frac{dz}{dx} \right) \right] \cos \left[\tan^{-1} \left(\frac{dz}{dx} \right) \right]$$

from above

$$A_1 = \frac{-2}{\pi} \int_0^\pi F(x) \cos \theta_0 d \theta_0$$

Substitute into equation B-6.

$$C_L = 2\pi \left[\frac{1}{\pi} \int_0^\pi F(x) d \theta - \frac{1}{\pi} \int_0^\pi F(x) \cos \theta d \theta \right]$$

$$C_L = 2\pi \left[\frac{1}{\pi} \int_0^\pi F(x) (1 - \cos \theta) d \theta \right]$$

expanding $F(x)$ and noting

$$\cos \tan^{-1} \left(\frac{dz}{dx} \right) = \cos \tan^{-1} \left(- \frac{dz}{dx} \right)$$

$$\sin (\theta_1 + \theta_2) = \sin \theta_1 \cos \theta_2 + \cos \theta_1 \sin \theta_2$$

$$F(x) = \cos \tan^{-1} \left(- \frac{dz}{dx} \right) \left[\sin \alpha \cos \left[\tan^{-1} \left(- \frac{dz}{dx} \right) \right] + \cos \alpha \sin \left[\tan^{-1} \left(- \frac{dz}{dx} \right) \right] \right]$$

Note

$$\sin \theta \cos \theta = 1/2 \sin 2 \theta$$

$$F(x) = \sin \alpha \cos^2 \tan^{-1} \left(- \frac{dz}{dx} \right) + 1/2 \cos \alpha \sin \left[2 \tan^{-1} \left(- \frac{dz}{dx} \right) \right]$$

substituting yields

$$C_l = 2 \left\{ \int_0^\pi (1 - \cos \theta) \left[\sin \alpha \cos^2 \tan^{-1} \left(- \frac{dz}{dx} \right) + 1/2 \cos \alpha \sin 2 \tan^{-1} \left(- \frac{dz}{dx} \right) \right] d\theta \right\}$$

With the above expression and a knowledge of the airfoil camber line the integral can be computed numerically and the approximate potential flow solution for a thin highly cambered airfoil obtained.

The P/W J57 15th stage blade profile was fitted to the following polynomials.

$$0 \leq \frac{x}{c} \leq .13559$$

$$\frac{z}{c} = -3.69107 \left(\frac{x}{c} \right)^2 + 1.62518 \left(\frac{x}{c} \right)$$

$$.13559 \leq x/c < .39831$$

$$\frac{z}{c} = -1.37997 \left(\frac{x}{c} \right)^2 + 1.12402 \left(\frac{x}{c} \right) + .025466$$

$$.39831 \leq x/c \leq 1.0$$

$$\frac{z}{c} = -.65337 \left(\frac{x}{c} \right)^2 + .49107 \left(\frac{x}{c} \right) + .16230$$

The solution obtained is given below

$$C_{\ell} = 4.724 \sin \alpha + 1.614 \cos \alpha$$

$$\alpha \mid C_{\ell} = 0 = -18.86^{\circ}$$

$$C_{\ell} \mid \alpha = 0 = 1.614$$

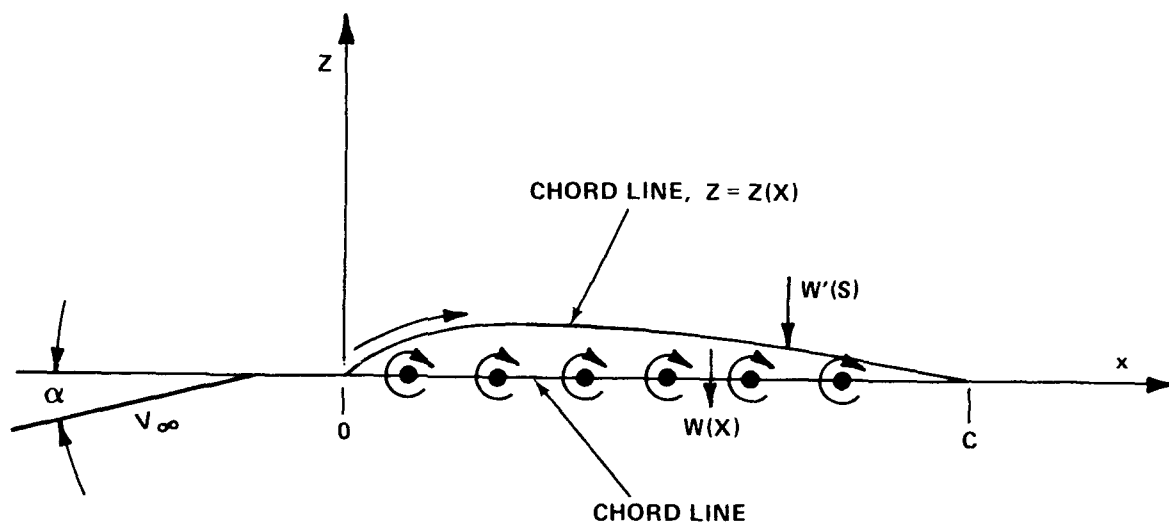


Figure 24. Placement of the vortex sheet for thin airfoil analysis.

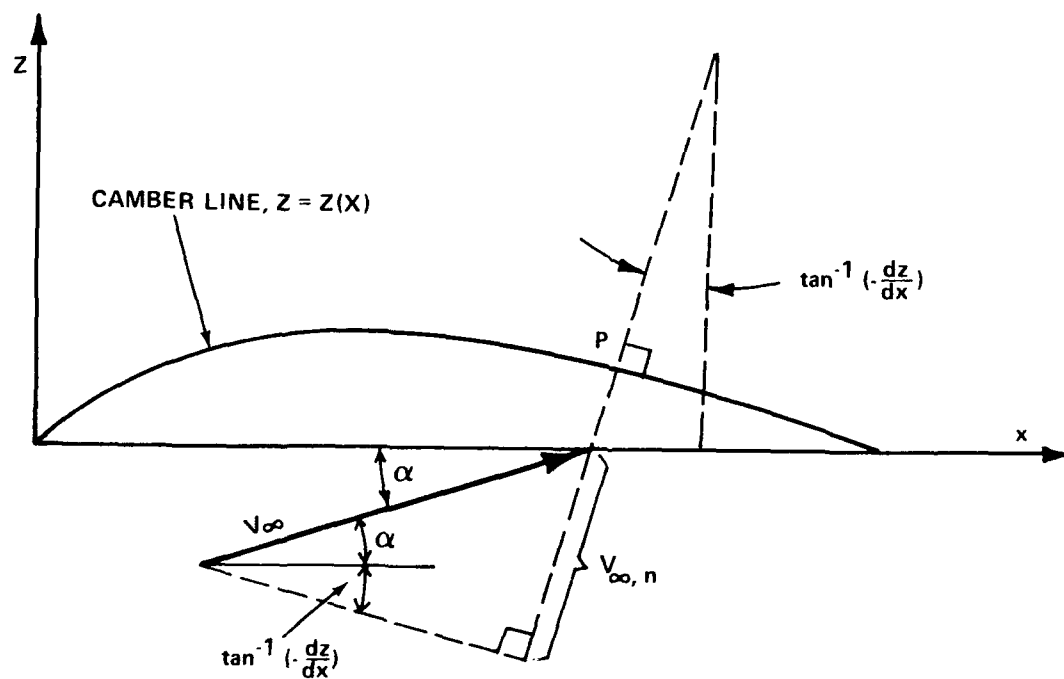


Figure 25. Determination of the component of freestream velocity normal to the camber line.

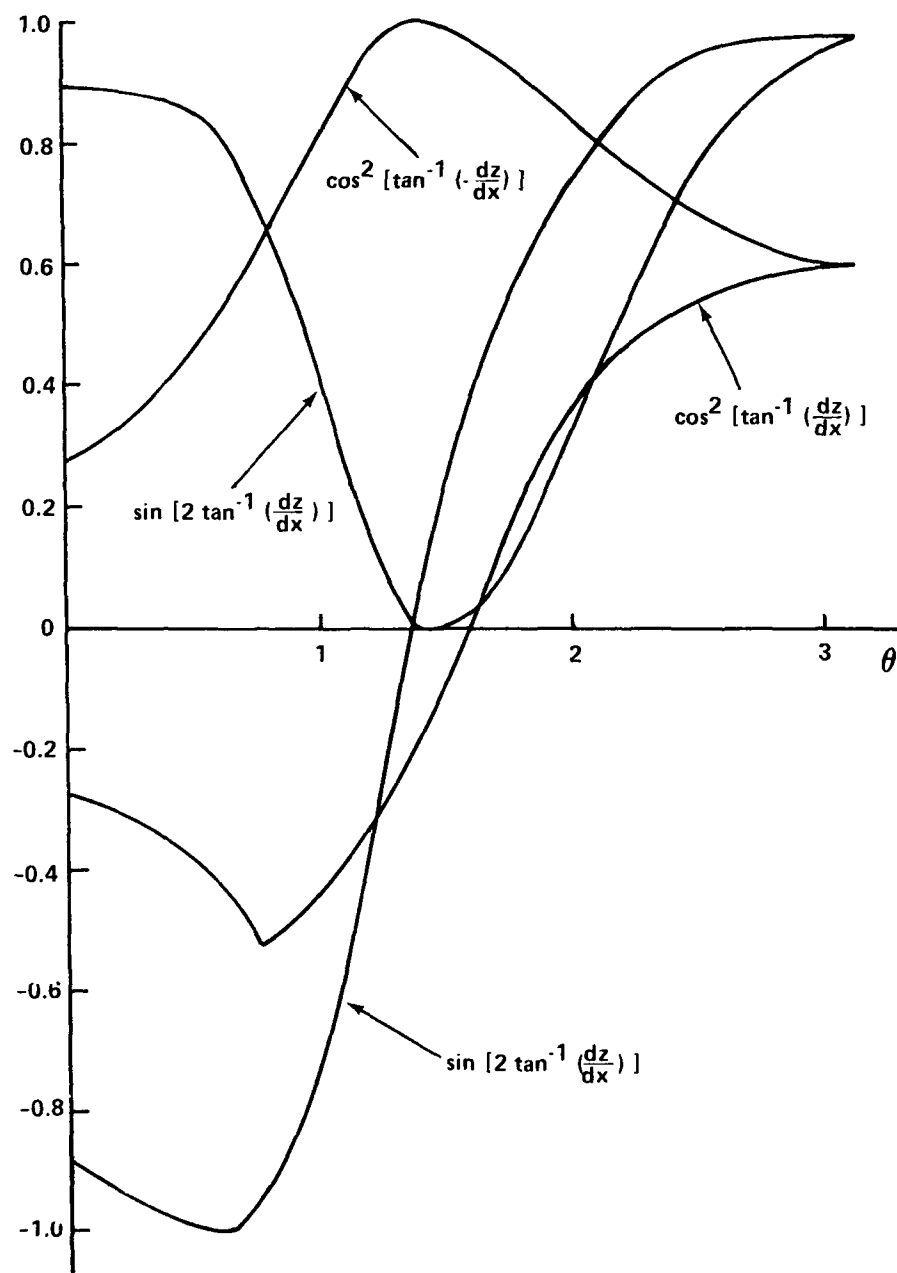


Figure 26. Computational results J57 profile.

APPENDIX C

DERIVATION OF COMPRESSOR EXIT PROPERTIES

In order to obtain a third equation and thus allow the calculation of density, velocity, and pressure at the exit, the second law of thermodynamics and the definition of polytropic compression efficiency were used.

$$\eta_{PC} = \frac{dT_{tis}}{dT_t} \quad (C-1)$$

Polytropic compression efficiency enables the formulation of total temperature rise from a known total pressure rise and overall compressor efficiency.

$$\frac{T_{t4}}{T_{t3}} = \left(\frac{P_{t4}}{P_{t3}} \right)^{\frac{\gamma-1}{\eta_{PC} \gamma}} \quad (C-2)$$

$$\eta_C = \frac{\left(\frac{P_{t4}}{P_{t3}} \right)^{(\gamma-1)/\gamma} - 1}{\left(\frac{P_{t4}}{P_{t3}} \right)^{(\gamma-1)/\gamma_{PC}} - 1} \quad (C-3)$$

The second law will relate the local static to local stagnation properties.

$$\frac{T_{t3}}{T_3} = \left(\frac{P_{t3}}{P_3} \right)^{(\gamma-1)/\gamma} \quad (C-4)$$

$$\frac{T_{t4}}{T_4} = \left(\frac{P_{t4}}{P_4} \right)^{(\gamma-1)/\gamma} \quad (C-5)$$

The thermodynamic equation of state for a perfect gas will relate static temperature to static pressure and density and allow the formulation of pressure in terms of density rise, polytropic efficiency, and total pressure rise.

$$T = P/\rho R \quad (C-6)$$

Substituting equations C-4 to C-6 into C-2 and rearranging yields equation C-7.

$$\left(\frac{P_{t4}}{P_{t3}} \right)^{\frac{(\gamma-1)(1-\eta_{PC})}{\gamma \eta_{PC}}} = \left(\frac{P_4}{P_3} \right)^{1/\gamma} \frac{\rho_3}{\rho_4} \quad (C-7)$$

Substituting equation C-7 and continuity into the definition of total pressure we arrive at an expression for the mean axial velocity at the compressor exit, equation C-8.

$$P_{t4} = \frac{PR^{\gamma^*} P_3 W^\gamma}{\rho_3^\gamma} V_4^{-\gamma} + 1/2 W V_4 \quad (C-8)$$

Where

$$W = \frac{\dot{m}}{A_4}$$

$$\gamma^* = \frac{(\gamma-1)(1-\eta_{PC})}{\eta_{PC}}$$

$$PR = \frac{P_{t4}}{P_{t3}}$$

From the solution of velocity the density may be computed from the continuity equation.

APPENDIX D NOMENCLATURE

a	erosion velocity exponent
B	ratio of bleed weight flow at compressor inlet
b	particle size exponent
C_D	cascade drag coefficient
C_l	blade lift coefficient
C_L	cascade lift coefficient
C_d	particle drag coefficient
C_x	axial velocity
c	chord
D_p	particle diameter
EPR	engine pressure ratio
EGT	exhaust gas temperature
$E(\Delta c)$	leading edge coefficient
$f(\alpha_p)$	dust angle of approach function
f	fuel-air ratio at combustor inlet
g	erosion function
H	total or stagnation enthalpy, Btu/lb
HPC	high pressure compressor
h	blade height
K	cascade modifying coefficient
L	cumulative mass of dust ingested
LPT	low pressure turbine
LPC	low pressure compressor
MRT	military rated thrust
\dot{m}	mass flow, (slugs/sec)

NOMENCLATURE (Continued)

N1	percent of LPC rotational speed
N2	percent of HPC rotational speed
N	number of stages
P	static pressure
P_t	total pressure
PR	total pressure ratio
PT7	total pressure at turbine exit
PLA	power level angle
PRS	surge pressure ratio
\bar{r}	hub-tip mean radius
r_t	tip radius
Re_p	particle Reynolds number
r_p	mean radius of particle
R	gas constant
SM	surge margin
s	cascade blade spacing
T	static temperature
TRT	takeoff rated thrust
T_t	total temperature
u	velocity
U	rotational speed
v	velocity
W	vertical velocity at camber line
w	weight flow
w_m	mean relative fluid velocity
x	distance along chord line

NOMENCLATURE (Continued)

z	height of camber line
α	airfoil angle of attack
β	relative fluid angle
γ	ratio of specific heats
δ	ratio of total pressure to NASA standard sea-level pressure at 2116 psi
ϵ	volume removed per particle impact
η	efficiency
θ	ratio of total temperature to NASA standard sea level temperature of 518.7°R
λ	tip clearance/blade height
μ	viscosity
ν	stagger angle
ξ	total pressure loss coefficient wrt. tip speed
ρ	density
ρ_r	reduced density
P	power of fan and/or accessories, Btu/s
τ	tip clearance
τ_v	particle relaxation time
ϕ	flow coefficient
ψ	total pressure coefficient
ω_e	fraction of blade height influenced

Subscripts

1	before impact
2	after impact
3	compressor inlet
4	compressor outlet

NOMENCLATURE (Continued)

i	cascade inlet
ii	cascade outlet
is	isentropic
L	loss
m	cascade mean fluid value
N	normal
o	uneroded
p	particle
pc	polytropic
T	tangential
t	tip
∞	free stream

DISTRIBUTION LIST

DEPARTMENT OF DEFENSE

ASSISTANT TO THE SECRETARY OF DEFENSE
ATOMIC ENERGY
ATTN: EXECUTIVE ASSISTANT

DEF RSCH & ENGRG
ATTN: ASD/C31 LT COL R DAVIS
ATTN: DIR CRUISE MISSILE SYS
ATTN: OSD/C31 LTC W RATHGABER
ATTN: STRAT & SPACE SYS(OS)
ATTN: STRAT & THEATER NUC FORCES

DEFENSE INTELLIGENCE AGENCY
ATTN: DB-6E V FRATZKE
ATTN: RTS-2B

DEFENSE NUCLEAR AGENCY
ATTN: SPWE
4 CYS ATTN: TITL

DEFENSE TECHNICAL INFORMATION CENTER
12 CYS ATTN: DD

FIELD COMMAND DEFENSE NUCLEAR AGENCY
ATTN: FCTXE
ATTN: FTTD W SUMMA

FIELD COMMAND/DNA
ATTN: FC 1

JOINT STRAT TGT PLANNING STAFF
ATTN: JK (ATTN: DNA REP)

DEPARTMENT OF THE ARMY

AVIATION APPLIED TECHNOLOGY DIRECTORATE
ATTN: DAVDL ATL-ATP(H MORROW)
ATTN: W SWINK

HARRY DIAMOND LABORATORIES
ATTN: SLCHD-NW P J GWALTNEY (20240)

U S ARMY AVIATION SYSTEMS CMD
ATTN: AMSAV ES (LTC DEVAUGHAN)

U S ARMY BALLISTIC RESEARCH LAB
ATTN: S POLYAK
ATTN: SLCBR TB B R RALEY

U S ARMY NUCLEAR & CHEMICAL AGENCY
ATTN: LIBRARY
ATTN: MONA NU MR LONG

DEPARTMENT OF THE NAVY

MARINE HELICOPTER SQUADRON ONE
ATTN: HMX-1/PLANS MAJ P HALTON

NAVAL AIR SYSTEMS COMMAND
ATTN: AIR 5164 J ALDRIDGE
ATTN: PM-23
ATTN: PMA-266E, MAJ HOLDSTEIN
ATTN: PMA-274
ATTN: PMA-275 V-22 DESK
ATTN: PMA-275M/JPI LTC SHERWELL

NAVAL RESEARCH LABORATORY
ATTN: CODE 2627 (TECH LIB)
ATTN: CODE 6006 D FORESTER

NAVAL WEAPONS CENTER
ATTN: CODE 3383 J MORROW

NAVAL WEAPONS EVALUATION FACILITY
ATTN: CLASSIFIED LIBRARY
ATTN: CODE 50 R TILLERY

OFC OF THE DEPUTY CHIEF OF NAVAL OPS
ATTN: OP 654(STRAT EVAL & ANAL BR)

STRATEGIC SYSTEMS PROGRAM OFFICE (PM-1)
ATTN: SP-272

DEPARTMENT OF THE AIR FORCE

AERONAUTICAL SYSTEMS DIVISION
ATTN: ASD/BIES E PRICE
ATTN: ASD/ENSS
ATTN: ASD/ENSSS H GRIFFIS
ATTN: ASD/YZE J DAY
ATTN: ASD/YZWT

AIR FORCE CTR FOR STUDIES & ANALYSIS
2 CYS ATTN: AFCSA/SAMI (R GRIFFIN)
ATTN: AFCSA/SASB
ATTN: AFCSA/SASM MAJ TOM HOPKINS

AIR FORCE FLIGHT TEST CENTER
ATTN: 6510 TESTW/TEV (K MARTIN)
ATTN: 6520 TESTG/TD (R HILDEBRAND)

AIR FORCE SYSTEMS COMMAND
ATTN: DLAJ
ATTN: DLWM
ATTN: SDNI

AIR FORCE WEAPONS LABORATORY, NTAAB
ATTN: NTA A SHARP
ATTN: NTATE E FRANKLIN

DNA-TR-86-306 (DL CONTINUED)

ATTN: NTN(NGCS) ATTN: SUL	DAYTON, UNIVERSITY OF ATTN: B WILT
AIR FORCE WRIGHT AERONAUTICAL LAB ATTN: GLXRM R DENISON	GENERAL ELECTRIC CO ATTN: H BEUTEL ATTN: M SUD
AIR FORCE WRIGHT AERONAUTICAL LAB ATTN: POTX M STIBICH	GENERAL MOTORS CORPORATION ATTN: R YORK
AIR UNIVERSITY LIBRARY ATTN: AUL-LSE	GENERAL RESEARCH CORP ATTN: D MIHORA ATTN: R CRAWFORD ATTN: W ADLER
DEPUTY CHIEF OF STAFF/AF-RDQM ATTN: AF/RDQM	INSTITUTE FOR DEFENSE ANALYSES ATTN: E BAUER
DEPUTY CHIEF OF STAFF/AF/RD-L ATTN: RD L	IRT CORP ATTN: D WOODALL
STRATEGIC AIR COMMAND ATTN: XOBBS ATTN: XOKF (MAJ A PHILPOTTS)	KAMAN SCIENCES CORP ATTN: D COYNE ATTN: L MENTE ATTN: R RUETENIK ATTN: W LEE
STRATEGIC AIR COMMAND/NRI-STINFO ATTN: NRI/STINFO	KAMAN SCIENCES CORP ATTN: J SOVINSKY
STRATEGIC AIR COMMAND/XPFS ATTN: XPFS	KAMAN SCIENCES CORP ATTN: E CONRAD
DEPARTMENT OF ENERGY	KAMAN TEMPO ATTN: DASAC
SANDIA NATIONAL LABORATORIES ATTN: TECH LIB 3141 (RPTS RECEIVING CLERK)	KAMAN TEMPO ATTN: DASAC
OTHER GOVERNMENT	LOCKHEED-CALIFORNIA COMPANY ATTN: A SCHUETZ ATTN: B OSBORNE
CENTRAL INTELLIGENCE AGENCY ATTN: OSWR/NED	LOCKHEED-GEORGIA COMPANY ATTN: A BENDERUD ATTN: R KELLY ATTN: T HODGSON
U S ARMS CONTROL & DISARMAMENT AGCY ATTN: H COOPER	MCDONNELL DOUGLAS CORP ATTN: H SAMS ATTN: R.J. PANDOLF
DEPARTMENT OF DEFENSE CONTRACTORS	MCDONNELL DOUGLAS CORP ATTN: J TRACY ATTN: L COHEN
AEROSPACE CORP ATTN: H BLAES	MCDONNELL DOUGLAS CORP ATTN: J MCGREW ATTN: M POTTER
BOEING CO ATTN: V SCHERER ATTN: A DACOSTA	
BOEING COMPANY, THE ATTN: N CARAVASOS	
BOEING MILITARY AIRPLANE CO ATTN: D SAWDY	
CALSPAN CORP 4 CYS ATTN: C PADOVA 4 CYS ATTN: M DUNN	
CARPENTER RESEARCH CORP ATTN: H J CARPENTER	

NORTHROP CORP
ATTN: C GUADAGNINO

PACIFIC-SIERRA RESEARCH CORP
ATTN: H BRODE, CHAIRMAN SAGE

R & D ASSOCIATES
ATTN: F A FIELD
ATTN: P RAUSCH
ATTN: T MAZZOLA
ATTN: T PUCIK

R & D ASSOCIATES
ATTN: B YOON

RAND CORP
ATTN: P DAVIS

RAND CORP
ATTN: B BENNETT

ROCKWELL INTERNATIONAL CORP
ATTN: A MUSICMAN
ATTN: P MASON
ATTN: S MELLINS

SCIENCE APPLICATIONS INTL CORP
ATTN: J COCKAYNE

SCIENCE APPLICATIONS INTL CORP
ATTN: A MARTELLUCCI

SOUTHERN RESEARCH INSTITUTE
ATTN: C PEARS
ATTN: S CAUSEY

SPARTA SYSTEMS, INC
ATTN: J DUBEL

TOYON RESEARCH CORP
ATTN: J CUNNINGHAM

UNITED TECHNOLOGIES CORP
ATTN: R FOULKROD

UNITED TECHNOLOGIES CORP
ATTN: J TARBOX

UNITED TECHNOLOGIES CORP
ATTN: J REED

